Investigation of the coherent $\gamma d \rightarrow \pi^0\pi^0\pi^0 d$ reaction at the BGOOD experiment

Richard Volk

Masterarbeit in Physik
angefertigt im Physikalischen Institut

vorgelegt der
Mathematisch-Naturwissenschaftlichen Fakultät
der
Rheinischen Friedrich-Wilhelms-Universität
Bonn

October 2024

I hereby declare that this thesis was formulated by myself and that no sources or tools other than those cited were used.

Bonn, ...

Date Signature

1. Gutachter: Prof. Dr. Hartmut Schmieden
2. Gutachter: Priv.-Doz. Dr. Tom Jude

Acknowledgements

I would like to thank Prof. Hartmut Schmieden for giving me the opportunity to work with such an interesting topic in a nice group and providing insightful comments at every stage of my work. I also thank Dr. Tom Jude for always helping me out with questions and code, Dr. Katrin Kohl for helping me with ExPLORA and whenever my code failed me, Antonio Figueiredo for again help with coding questions and discussions about various topics, Johannes Groß for answering my questions about hardware-related topics, Mrunmoy Jena for many talks about either of our works which were always interesting and Vlera Hajdini for providing such a nice atmosphere in the office and talking about everything that came up.

Contents

CHAPTER 1

Introduction

The history of sub-atomic physics began in the last decades of the 19th century with the first indications that atoms are not, as their name suggests, "indivisible", but must possess a further structure. After Rutherford's famous experiment showed the atomic nucleus' existence, the basic composite structure of atoms was established. The development of quantum mechanics allowed for a description of the electron shell and its associated energy levels. The nucleus was later discovered to consist of protons and neutrons, bound together by the nuclear force.

The nuclear force was described by Yukawa who first proposed that it should be quantized and showed the properties of its mediator particle. It was named *meson* since its mass fell between the electron and proton mass. From cosmic ray experiments later the pion was found to be Yukawa's particle, possessing the properties he calculated. With first accelerators the discovery of antiparticles like the antiproton and antineutron was possible, validating Dirac's relativistic quantum theories. Neutrinos were first theorized as a solution to the problem of energy distribution of electrons in beta decays: instead of having a fixed energy, like one would expect of a two-body decay, their energy was spread out. A new particle, the neutrino, that would remain undetected would solve this problem. But the direct observation of the neutrino proved to be difficult and only in the mid 1950's their existence was confirmed.

Apart from the fact that muon and muon-neutrino seemed essentially "unneeded" for the description of matter another problem was soon discovered: New mesons like the K^0 and K^+ were found, later the η, ω and more. Also baryons like the Λ's, Σ's, Ξ's and Δ's were discovered. All of them were unexpected but some even behaved "strangely" as they seemed to change direction mid-flight, forming a "V" like path. Only later it was discovered that this was due to weak decays and unobserved neutrinos. The strange quark was named after these "strange" particles, as it was the reason for their weak decay. But still there were many more particles than what was "needed" to construct basic everyday matter and there seemed to be no order or reason to them.

In this situation it were Gell-Mann and Zweig who independently managed to find a way to solve this problem: the constituent quark model. By using group theory they found that baryons and mesons could be constructed of respectively three quarks and a quark-antiquark pair. One could then sort the particles into multiplets (like the baryon octet) and even predict some which were not discovered back then. The force which binds these quarks to form the hadrons was named the strong force and the corresponding charge is called color. There are three (green, blue, red) colors as well as three anti-colors (anti-green, anti-red, anti-blue) and any observed particle is white, or color-neutral, an

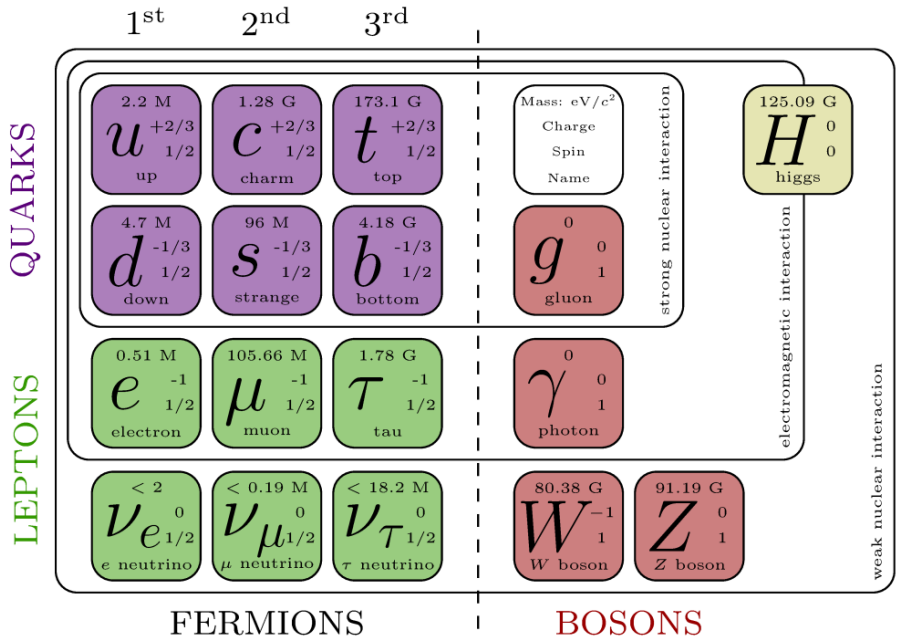

Figure 1.1: Overview over the particles of the Standard Model, taken from [2]

effect which is called *color confinement*.

Later it was found that this is only an approximation: Inside the particles there are also sea quarks which are created in particle-antiparticle pairs from the strong field and do not contribute to the particles quantum numbers as opposed to the valence quarks.

With the discoveries of more particles, like the charmed and bottom hadrons and the tau lepton and its accompanying neutrino as well as the vector bosons $W^{\pm}$ and Z the *Standard Model* (SM) of particle physics was developed [1].

It describes the forces between elementary particles via the principles of gauge-theories and symmetry-breaking. In total three such forces (electromagnetic, weak and strong) are present in the SM and describe the interactions between 6 quarks, 6 leptons and 5 gauge bosons (see fig. Fig. 1.1). The gauge theory which describes the interaction between electrically charged and magnetic particles is *quantum electrocynamics* (QED) and the electromagnetic force is mediated by the photon. This was unified by Glasgow, Salam and Weinberg with the weak interaction, which is mediated by the W and Z bosons, to form the electroweak theory. *Quantum chromodynamics* (QCD) describes the interactions between quarks and the strong force is mediated by 8 gluons. Together with the Higgs boson, which gives the particles mass via *spontaneous symmetry breaking* these theories form the SM.

Since Gell-Mann and Zweig presented their theories it was already clear that there could be bound colorless particles consisting of four, five or six (anti-)quarks and early quark models predicted the existence of such objects where the constituent quarks could be bound by the strong force. Such a particle was already known, the deuteron is a dibaryon, a bound system of two baryons (proton and neutron). In the "rush era" from the 1970s to the 1990s many experiments searched for further dibaryons and many claims were made, but with the arrival of better accelerators and detectors and in consequence better statistics, most of these claims were proven false [3].

Recently interest in these states was renewed with the observation of the $d^*(2380)$ dibaryon state

by the WASA-at-COSY collaboration in 2014 [4]. It was observed in the nucleon fusion channels $np \rightarrow d\pi^0\pi^0$ and $np \rightarrow d\pi^+\pi^-$, which implies it could also be present in photoproduction channels. The ELPH collaboration published results on the $\gamma d \rightarrow \pi^0\pi^0 d$ reaction which show interesting structures in the cross section measured, which could be hints for further dibaryon states [5] [6]. The BGOOD collaboration published also results on this channel [7] and also a paper on the $\gamma d \rightarrow \eta\pi^0 d$ is in preparation [8], both of which show further interesting results. This motivates a closer look at the photoproduction reaction $\gamma d \rightarrow \pi^0\pi^0\pi^0 d$ which is analyzed in this thesis. The aim is to measure the differential cross section of the reaction with data from the BGOOD experiment and the differential cross section with respect to the invariant mass distribution of $\pi^0\,\pi^0$, $\pi^0\,\pi^0\,\pi^0$, $\pi^0 d$ and $\pi^0\pi^0 d$ in order to investigate possible structures similar to the ones observed in the previous papers.

In the following, Chapter 2 explains the motivation and physics background in more detail. Chapter 3 shows the experimental setup of the BGOOD detector in so far as it is relevant for the thesis. Chapter 4 describes the analysis procedures used for extraction of the cross sections. In Chapter 5 a comparison of the cross sections with previous results and possible interpretations is given, as well as a summary of the thesis.

CHAPTER 2

Motivation

The spectrum of hadronic states and further physical attributes were first explained by the so-called *eightfold way*, a model named such after a buddhist concept by Gell-Mann, which originates from group theoretical considerations. This model led to predictions of further hadronic particles and states but also more exotic particles such as dibaryons. This chapter introduces the physical background of the thesis beginning with the quark multiplets of the eightfold way in Section 2.1, continuing with the underlying quark model in Section 2.2. The proton, neutron and deuteron are described in a bit of detail in Section 2.3. In Section 2.4 the first prediction of dibaryons by Dyson and Xuong is shown and in Section 2.5 the first searches are briefly described. Section 2.5.1 shows the observation of the first dibaryon state, while Section 2.5.2 and Section 2.5.3 describe the photoproduction experiments and their results at ELPH and BGOOD respectively.

2.1 The Eightfold Way

Gell-Mann discovered the concept by which one can structure the mesons and baryons with group theory [9]. The model was purely phenomenological in the beginning and was developed to bring order in the vast number of hadronic particles discovered. It was therefore not accepted in the beginning, but after it's prediction of the Ω^- baryon was discovered to be true, it gained more traction among the physicists [1].

The model itself is simple: Mesons and Baryons are ordered into groups by their angular momentum J and parity P. These groups are called multiplets and can be further structured by their isospin z-component I_3 and hypercharge Y which is defined as $Y = \mathcal{B} + S - \frac{C-B+T}{3}$. Here $\mathcal{B}$ is the baryon number, S the strangeness, C the charm, B the bottomness and T the topness. Mesons have a baryon number of $\mathcal{B} = 0$, while baryons have $\mathcal{B} = 1$. Strangeness, charm and bottomness depend on the quark content of the meson, see section Section 2.2 for the quarks' quantum numbers. The diagrams in Fig. 2.1 shows the multiplets for the lighter mesons including the π^0 with isospin $I = 0$ which is relevant for his work. In Fig. 2.2 the baryons' equivalent multiplets are shown, where also the ground state nucleons, n and p, are found which compose the deuteron d. It should be noted that while this model works remarkably well for light quarks (u, d, s), for heavier ones like the c this is not as accurate. This is due to the fact that light quarks are nearly mass degenerate but the charm already has a mass of 1.27 GeV. So while one can make multiplets for charmed mesons and baryons like in Fig. 2.1 and

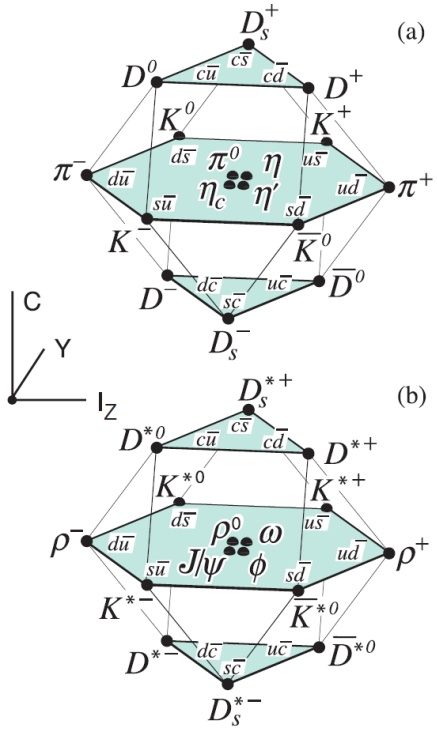

Figure 2.1: The multiplets of light and charmed mesons where (a) shows the pseudoscalar $J^P = 0^-$ and (b) the vector mesons $J^P = 1^-$. In the center plane the light meson nonets can be found with the charmonium ($c\,\bar{c}$) states added. Figure taken from [10].

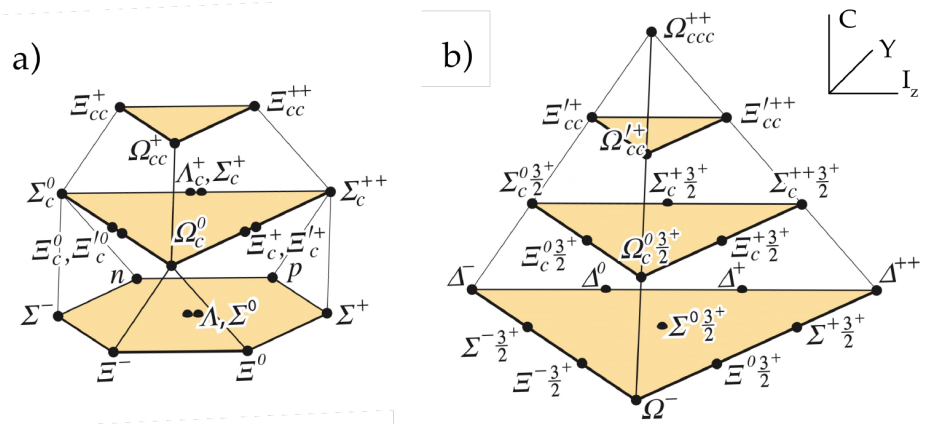

Figure 2.2: The baryon ground state multiplets of light and charmed baryons where (a) shows the $J^P = \frac{1}{2}^+$ states and (b) the $J^P = \frac{3}{2}^+$ ones. The lowest plane show the baryon octet and decuplet respectively. Figure taken from [10].

Fig. 2.2, they are not as useful as the light quark multiplets [10].

2.2 The Constituent Quark Model

In 1964 Gell-Mann [11] and Zweig [12] independently developed the quark model which gave a physical reason to the purely phenomenological model from before. Baryons and mesons are in this model made up by point-like particles called quarks with a new charge, *color*, which can be blue, red

	d	u	s	c	b	t
Q	$-\frac{1}{3}$	$+\frac{2}{3}$	$-\frac{1}{3}$	$+\frac{2}{3}$	$-\frac{1}{3}$	$+\frac{2}{3}$
I	$\frac{1}{2}$	$\frac{1}{2}$	0	0	0	0
I_z	$-\frac{1}{2}$	$+\frac{1}{2}$	0	0	0	0
S	0	0	-1	0	0	0
C	0	0	0	+1	0	0
B	0	0	0	0	-1	0
T	0	0	0	0	0	+1

Table 2.1: Quantum numbers of quarks. See [10]

or green, bound together by the strong force. Gluons g are the exchange bosons of this force and the effect that quarks are never observed free is called *confinement*. According to it, all observed particles need to be color-neutral, so they need to contain either all colors in equal amounts or have no color charge. The latter is possible because anti-quarks possess anti-color charges like anti-red, anti-blue and anti-green. Baryons are in this model made up of 3 constituent quarks and mesons of a quark-antiquark pair [1].

The Table 2.1 shows all today known quarks and their quantum numbers. For anti-quarks the sign simply changes on all of them. The symbols (d, u, s, c, b, t) abbreviate the names: *down, up, strange, charm, bottom, top*. As all quarks have a baryon number of $\mathcal{B} = \frac{1}{3}$ and this is an additive quantum number, one sees easily how baryons have $\mathcal{B} = 1$ and mesons $\mathcal{B} = 0$, reproducing what was described in Section 2.1. Every quark has a spin of $\frac{1}{2}$, making them fermions. Consequently, baryons have half-integer spins, mesons integer-spin particles and dibaryons, since they consist of two baryons, add up to an integer spin, making them bosons [10].

In this model one can use group theory and derive approximate wave functions of the particles by using the quarks' own wave function. This is important because even in this model, some particles aren't simple combinations, which is also true for the neutral pion which is a mixture of up-antiup and down-antidown states:

$$\left|\pi^0\right\rangle = \frac{1}{\sqrt{2}}\left(\left|u\bar{u}\right\rangle - \left|d\bar{d}\right\rangle\right)$$

Measurements give a rest mass of (134.9768 ± 0.0005) MeV[1] and the main decay mode is a two-photon decay $\pi^0 \rightarrow \gamma\gamma$ with a branching ratio of (98.823 ± 0.034) % [10].

2.3 The proton, neutron and deuteron

The only baryons playing a role in the reaction investigated in this thesis are the proton ($u\ u\ d$) and neutron ($u\ d\ d$), the lowest lying ground-state baryons with a rest mass of 938.27 MeV for the proton and 939.57 MeV for the neutron[2] [10]. Referencing table Table 2.1 it is easily seen that the proton has an electric charge of $Q = +1$ and an isospin $I = \frac{1}{2}$, $I_z = +\frac{1}{2}$ while the neutron has $Q = 0$, $I = \frac{1}{2}$ and

[1] This thesis uses natural units, where $c = \hbar = 1$, which simplifies mass, momentum and energy units, so e.g. mass is measured in MeV instead of MeV/c^2

[2] These measurements have of course uncertainties, but since both are of the order of 10^{-9}MeV they are negligible in the context of BGOOD's precision

State	Mass [MeV]	Baryon configuration
D_{01}	1 876	$p\,n$ (deuteron)
D_{10}	1 876	${}^1S_0 NN$ (virtual state)
D_{12}	2 160	$\Delta\, N$
D_{21}	2 160	$\Delta\, N$
D_{03}	2 350	$\Delta\, \Delta$
D_{30}	2 350	$\Delta\, \Delta$

Table 2.2: Dyson and Xuong's diabryon sextuplet. Besides the confirmed deuteron and the virtual state all other particles, masses and configurations are predictions. See [13].

$I_z = -\frac{1}{2}$.

The deuteron is a bound $p\,n$ system with rest mass 1 875.61 MeV [10] and a binding energy of approximately 2.2 MeV [3], which compared to other nuclei is rather low.

2.4 Dibaryon multiplet by Dyson and Xuong

Freeman J. Dyson and Nguyen-Huu Xuong published a paper in 1964, in which they predicted a sextuplet of non-strange dibaryons with the same group theoretical considerations which gave rise to the hadrons, only here used on 6 quarks [13]. This model gives rise to a sextuplet of dibaryon states, named D_{IJ}, where I is the isospin and J the total angular momentum. The Table 2.2 shows Dyson and Xuong's predictions for these states. As shown there, the D_{01} is the ground-state deuteron and its mass was already known. The D_{10} state is a virtual ${}^1S_0$ state which was already identified in final state interactions of low-energy nucleon-nucleon scattering [3].

Since both of these states have approximately the same mass, the model prediction was that interchanging spin and isospin values should not change the mass of the dibaryon states. The next two states D_{12} and D_{21} were predicted to be near the $\Delta\, N$ threshold with the D_{21} being isospin ($I = 2$) decoupled from the nucleon-nucleon system.

The states with the highest mass, D_{03} and D_{30}, were predicted with a rest mass of 2 350 MeV, so ca. 110 MeV below the $\Delta\, \Delta$ threshold. The isoscalar D_{03} should couple to proton-neutron systems and due to the branching ratios of the Δ a preferred decay would be like $np \rightarrow D_{03} \rightarrow NN\pi\pi$ [3]. This was observed in the reaction $pn \rightarrow d\pi^0\pi^0$ at the WASA detector [14]. The D_{30} can only be observed when at least two more pions are present in $N\,N$ collisions, since its isospin would suppress the production otherwise [3].

It should be noted however, that Dyson and Xuong's sextuplet predicted not the deuteron in the strict sense of the word. Sine they used quarks and group theory, their prediction essentially worked with color-bound objects, just like three quarks formed a baryon. The deuteron is a bound proton-neutron system where the effective degrees of freedom are the nucleons, which are bound by pion exchange. In this sense, associating the deuteron with Dyson and Xuong's D_{01} is not exactly accurate.

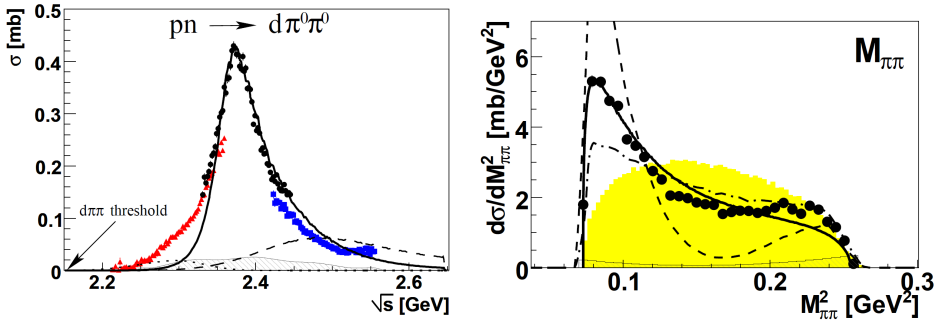

Figure 2.3: (Differential) cross sections for the $pn \rightarrow d\pi^0\pi^0$ reaction measured by the WASA-at-COSY collaboration. Left: Total cross section together with a s-channel resonance fit with $m = 2.37\,\text{GeV}, \Gamma = 68\,\text{MeV}$ (solid line). Right: Differential cross section at $\sqrt{s} = 2.38\,\text{GeV}$. Curves are s-channel resonance decaying into $\Delta\,\Delta$ calculations. Shaded yellow shows pure phase space, data in black circles. Figures taken from [14].

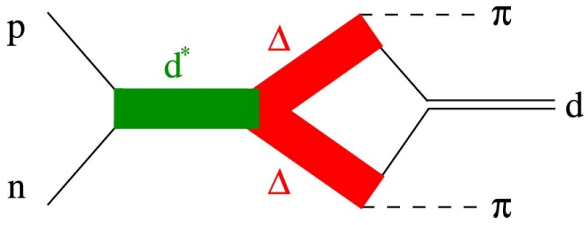

Figure 2.4: Decay of $d^*(2380)$ into an intermediate $\Delta\,\Delta$ system before decaying into a double-pionic fusion. Figure taken from [15].

2.5 Dibaryon research in recent years

The quark model does not forbid observable particles with 4 or more constituent quarks. The restriction only lies in the neutral color charge as mentioned in Section 2.2 and QCD also does not exclude further combinations. Dibaryons were a theoretical construct since the neutron was discovered in 1932 but further supported by the quark model in the 1960s [3]. Nevertheless it took until 2014 to observe what is called the first "excited" dibaryon state, the $d^*(2380)$ at COSY [4]. Further searches in photoproduction experiments like ELPH and BGOOD delivered unexpected results in channels like $\gamma d \rightarrow \pi^0\pi^0 d$.

2.5.1 d*(2380) observation at COSY

First hints for the $d^*(2380)$ were obtained by the WASA-at-COSY collaboration in 2011 in the measurement of the total cross section of the double-pionic-fusion reaction $pn \rightarrow d\pi^0\pi^0$ [14]. Fig. 2.3 shows the total cross section on the left where a resonance-like peak is observed at $\sqrt{s} = 2.37\,\text{GeV}$. Also a low mass enhancement in the invariant $\pi^0\,\pi^0$ mass distribution, the ABC[3] effect, can be observed in Fig. 2.3 on the right. The solid line is a calculation of the decay of $d^*(2380)$ into a $\Delta\,\Delta$ system with $J^P = 3^+$ and form factor. This decay can be seen schematically in Fig. 2.4 with a subsequent decay of the two Δ's into two pions and fusion of the two nucleons into a deuteron. This shows a possible connection between the ABC effect and the $\Delta\,\Delta$ system from the $d^*(2380)$, but in the non-fusion reaction $np \rightarrow np\pi^0\pi^0$ there is no ABC effect observed [15].

[3] Named such after the authors Abashian, Booth and Crowe who first published measurements which showed the effect [16].

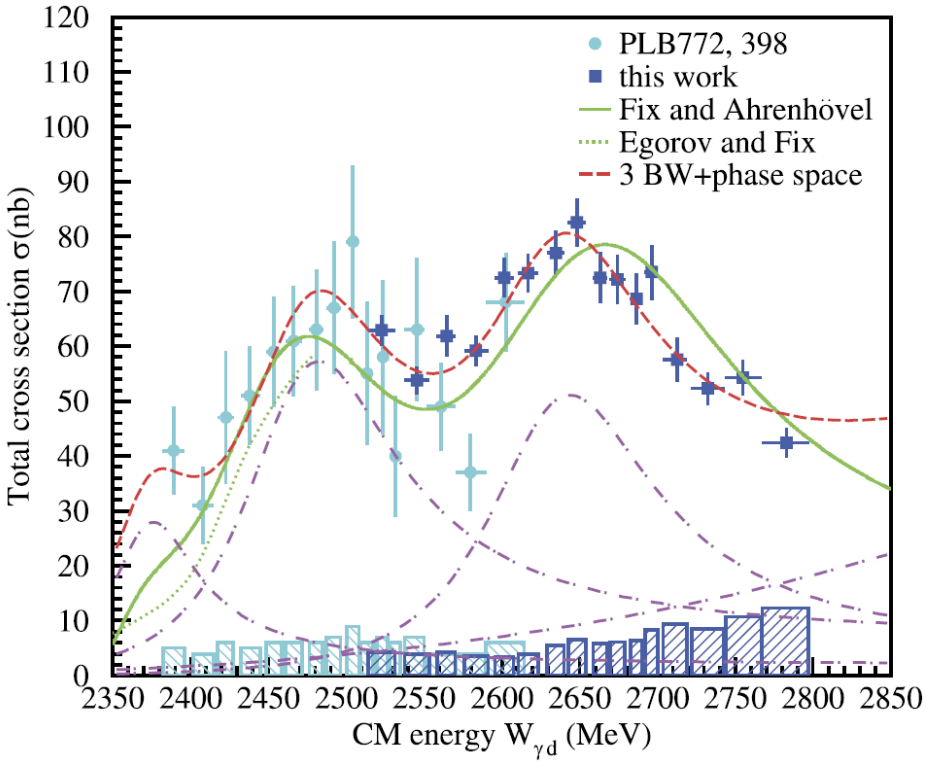

Figure 2.5: Total cross section of the coherent $\gamma d \to \pi^0\pi^0 d$ reaction from ELPH. Model calculations by Fix and Ahrenhövel [17] and Egorov and Fix [18] are shown as well as a Fit with 3 Breit-Wigner Peaks and a phase space contribution. Figure taken from [6]

This was further confirmed when the collaboration could observe the $pn \to d\pi^+\pi^-$ reaction and measure polarization observables, calculating a pole in ${}^3D_3 - {}^3G_3$ waves which supports the resonance hypothesis. Since the mass 2.38 GeV was close to Dyson and Xuong's predictions and the resonance was consistent with $I(J^P) = 0(3^+)$ it was assigned to be the D_{03} state as mentioned in Section 2.4.

2.5.2 Coherent photoproduction of light mesons at ELPH

The ELPH experiment situated at the Tohoku University searched for dibaryons in photoproduction channels. The coherent $\gamma d \to \pi^0\pi^0 d$ reaction was studied to observe possible intermediate states. First results in 2017 measured the total cross section for the center-of-mass energy interval W = 2.38–2.61GeV and gave an upper limit of 0.034 µb to the cross section for the $d^*(2380)$ resonance [5]. In a further publication in 2019 the energy range was extended up to W = 2.8 GeV and the cross section showed hints for an isovector dibaryon at (2.14 ± 0.01) GeV in the $\pi^0 d$ and two isoscalar dibaryons at 2.47 GeV and 2.63 GeV in the $\pi^0\pi^0 d$ channel [6]. Furthermore the measured angular distribution of the two π^0's limited the isovector to $J^P = 1^+, 2^+, 3^-$. While the theoretical models by Fix and Ahrenhövel [17] and Egorov and Fix [18] work well to reproduce the cross section as seen in Fig. 2.5, both cannot explain the deuteron emission angular behavior (see Fig. 2.6) [6].

Further the coherent $\gamma d \to \pi^0\eta d$ reaction was measured to observe angular distributions and invariant mass spectra [19]. Again the total cross section was measured and for this reaction the data

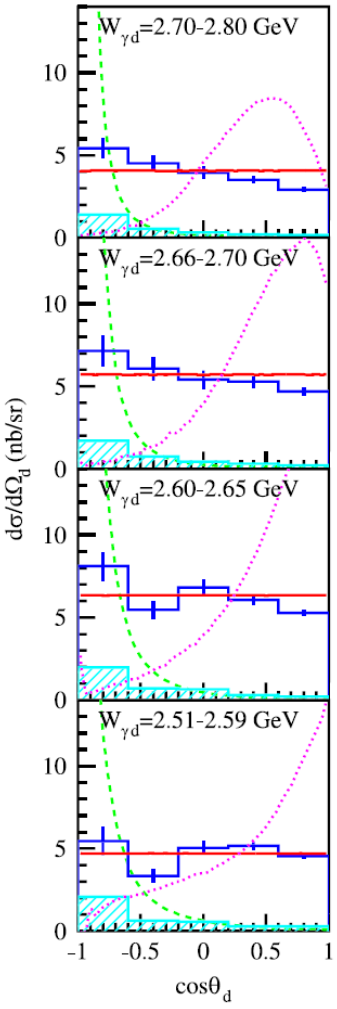

Figure 2.6: Differential cross sections $\frac{d\sigma}{d\Omega_d}$ for different center-of-mass energies. The dashed green line shows the calculation by Fix and Ahrenhövel [17], the solid red the pure phase space and the dotted magenta one represents a semi-quasi-free process. Figure taken from [6].

agreed well with model calculations by Fix and Egorov [20] and another one by Egorov [21] when they include final state interactions as seen in Fig. 2.7, but as before the angular distributions of the deuteron in particular could not be reproduced by the same models. The $M_{\eta d}$ and $M_{\pi d}$ invariant mass spectra were measured and showed an increased differential cross section $\mathrm{d}\sigma/\mathrm{d}M_{\eta/\pi d}$ near the ηd threshold, see Fig. 2.9. The spectra were fitted with two amplitudes from a phenomenological model by the ELPH collaboration where intermediate quasi-two-body states were used to model the differential cross sections. Approximate reaction mechanisms of this phenomenological model are shown in Fig. 2.8 and their fit matches the data quite well as seen in Fig. 2.9. From these fits a pole can be extracted but it is unclear whether or not the ηd state is bound or virtual due to an unclear sign, but the authors estimate it should be a virtual one.

Both reactions showed in the analysis of the ELPH collaboration interesting results and there are some commonalities: The total cross section can be fit well with conventional models but they fail at the differential cross sections $\mathrm{d}\sigma/\mathrm{d}\Omega_d$. This is even more pronounced as models expect a peak in the backward direction and a sharp drop while going forward because as explained in Section 2.3 the deuteron is only loosely bound and to reach forward directions a large momentum transfer is needed

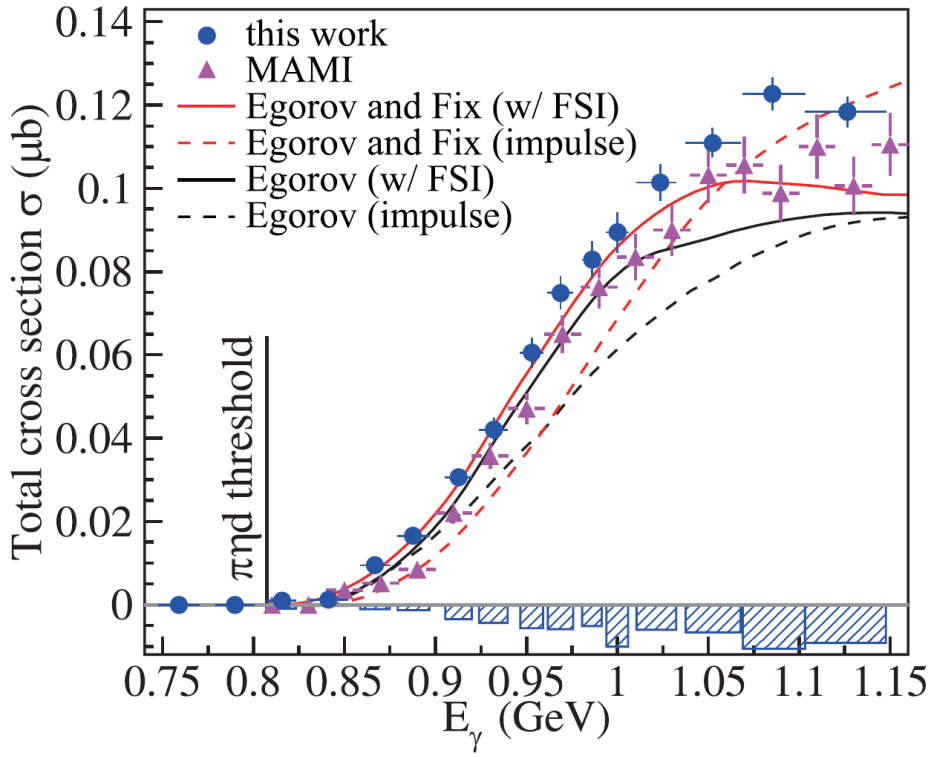

Figure 2.7: Total cross section of the coherent $\gamma d \rightarrow \pi^0 \eta d$ reaction with calculations by Egorov and Fix [20] and Egorov [21]. Figure taken from [19].

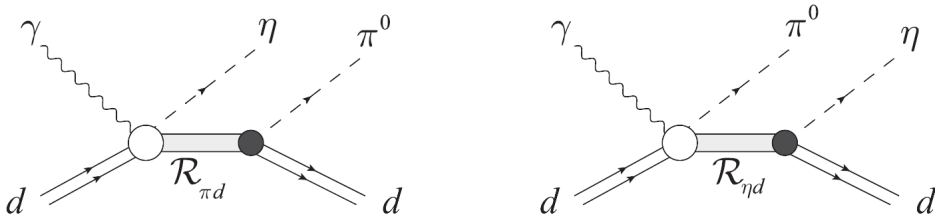

Figure 2.8: Reaction mechanisms used for calculating model fits by the ELPH collaboration. Figure taken from [19].

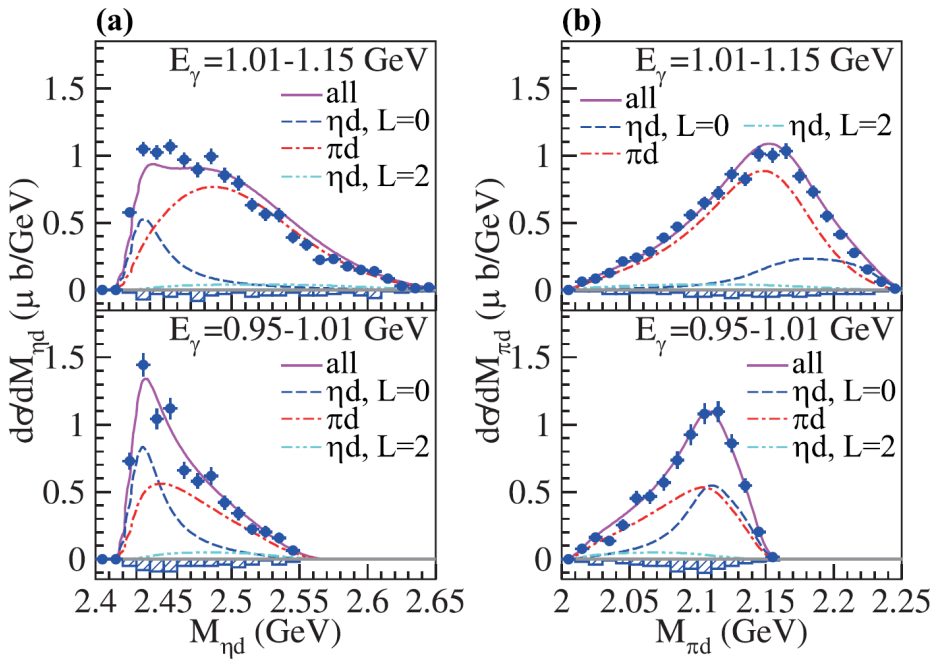

Figure 2.9: Invariant mass spectra $M_{\eta d}$ (a) and $M_{\pi d}$ (b) for the coherent $\gamma d \rightarrow \pi^0 \eta d$ reaction. Blue dots represent data from ELPH while lines show various intermediate dibaryon resonance model fits. Figure taken from [19].

which should break the deuteron up. Instead a rather consistent diff. cross section is observed with only a small drop (e.g. in Fig. 2.6) while going to forward direction. Since the BGOOD experiment can identify forward-going deuterons (for more specifics on the BGOOD experiment see Chapter 3) the investigation of both reactions was motivated.

2.5.3 Coherent photoproduction of light mesons at BGOOD

In 2022 a paper was published by the BGOOD collaboration which analyzed the coherent $\gamma d \rightarrow \pi^0 \pi^0 d$ reaction at forward deuteron angles $\cos\theta^d_{\mathrm{CM}} > 0.8$ [7]. After a full kinematic reconstruction, the deuteron was identified directly in the forward spectrometer and pions were observed in the central calorimeter via the decay $\pi^0 \rightarrow \gamma\gamma$. The differential cross section $\mathrm{d}\sigma/\mathrm{d}\Omega$ was then extracted and compared to model calculations.

In Fig. 2.10 the model by Fix, Ahrenhövel and Egorov [17][18] is compared, but even after scaling it by a factor of 5 it still is too low in amplitude and not fitting in shape in comparison to the measurement. A toy pickup model (see [7] for more detail) is also shown but it suffers from similar problems. The measurde diff. cross section was observed to be too high in strength, in particular since the deuteron is here measured in very forward angles.

A fit was also made by summing phase space terms and 3 Breit-Wigner functions, one of which is the $d^*(2380)$ and the other two are the isovector dibaryon candidates of the ELPH paper [6]. While the fit as seen in Fig. 2.11 is consistent with the data, a remark was made by the authors that any small enhancement at low center-of-mass energies W could still be made by variations of the used toy pickup model and the fit also is made with limited statistical precision of the data and resolution in W. They also add that One-Pion-Exhange (OPE) models driven by triangle singularities could explain the diff. cross section but no calculation was yet made [7]. However similar models which have peaks in the πd and $\pi\pi d$ region were made [22][23], but limited experimental precision prevents confirmation [7].

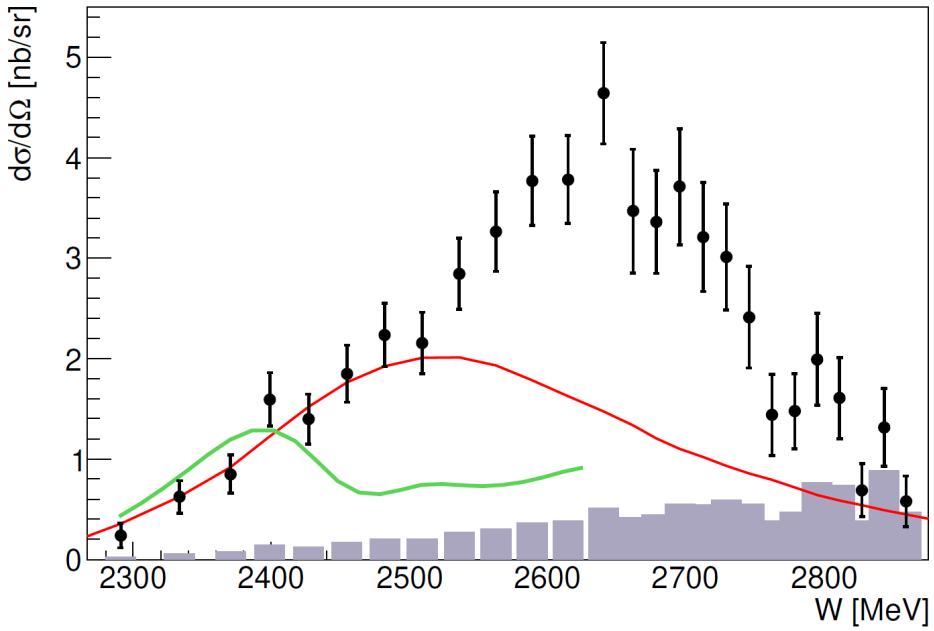

Figure 2.10: Differential cross section for coherent $\gamma d \rightarrow \pi^0\pi^0 d$ with the calculation by Fix, Ahrenhövel and Egorov [17] [18] scaled by ×5 and a toy pickup model at arbitrary scale (for more information see reference). Figure taken from [7].

For higher energies $W > 2.5\,\text{GeV}$ in the $\pi^0 d$ invariant mass spectrum a two-peak structure was observed which the authors propose could be caused by sequential dibaryon decay mechanism which was also fitted, but although the mass of 2 114 MeV was close to the 2 140 MeV of one candidate by ELPH, the width of 20 MeV was much narrower than ELPH's 91 MeV.

A paper from BGOOD which at the time of this thesis is still in preparation, also analyzed the coherent $\gamma d \rightarrow \pi^0\eta d$ reaction and the differential cross section for forward deuteron angles $\cos\theta^d_{\text{CM}} > 0.8$ was extracted after a kinematic reconstruction and after subtracting quasi-free production off protons [8].

Additionally a fit for kinetic models, where two excited nucleon states which interact via pion exchange emit the π^0 and the η before coalescing into a deuteron again was made. Fig. 2.12 shows that these fits were generally consistent with the data, but statistical precision especially for higher energies W is limited.

The invariant mass distribution of ηd was consistent with the phenomenological model by the ELPH collaboration [19] but it seems the relative momentum was too large to consider a bound ηd system for the low mass enhancement. Even at its lowest the relative momentum was observed to have a mean of 526 MeV [8]. The $\pi^0 d$ and $\pi^0\eta$ invariant mass distributions were observed to be consistent with ELPH's observations and support the isovector dibaryon candidate at 2.15 GeV however even after its threshold, no structure which could be caused by the $a_0(980)$ was observed.

Both BGOOD papers show a reasonable agreement with the dibaryon candidates proposed by the ELPH collaboration, the most notable disagreement being difference in width of about 70 MeV for the 2.14 GeV candidate. In both reactions however, alternative models were also proposed and it could be seen that with the current limits in statistics and precision no clear argument for one alternative can be made.

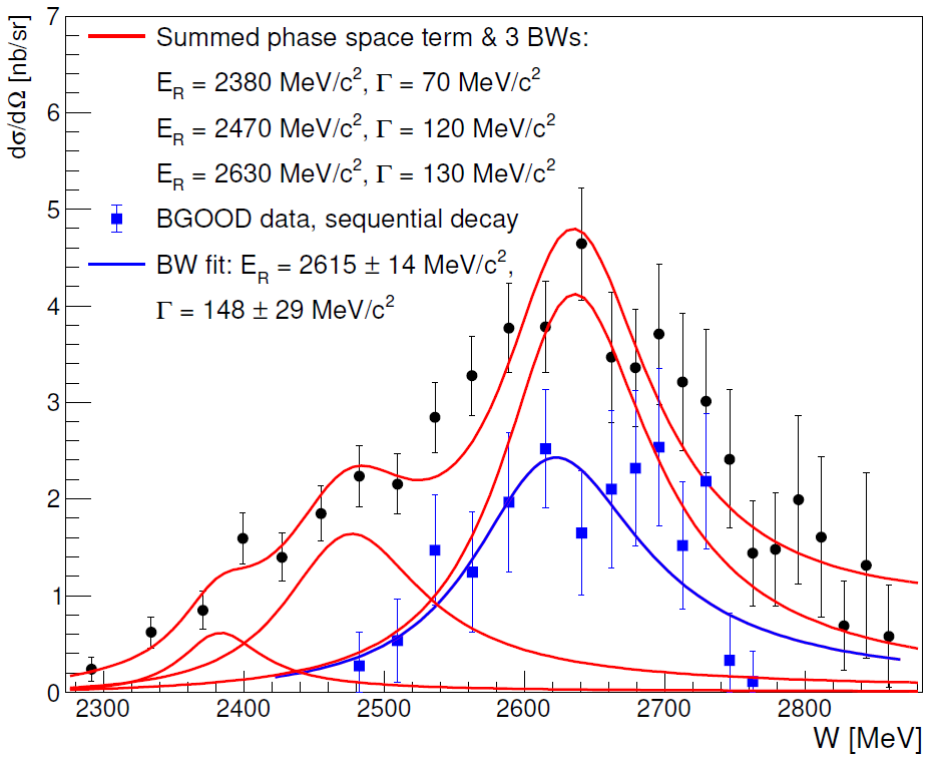

Figure 2.11: Differential cross section for coherent $\gamma d \rightarrow \pi^0\pi^0 d$ with a fit of 3 Breit-Wigner functions and extraction of sequential decay. Figure taken from [7].

All of this motivates a look into the coherent $\gamma d \rightarrow \pi^0\pi^0\pi^0 d$ reaction. While being similar to the other two reactions in that it is the coherent photoproduction of light, non-strange pseudoscalar mesons off a deuteron, the additional pion produced means that the isospin in the reaction is greater by 1 when compared to $\gamma d \rightarrow \pi^0\pi^0 d$ (for π^0 isospin is $I = 1$ [10]), possibly allowing access into different modes previously suppressed.

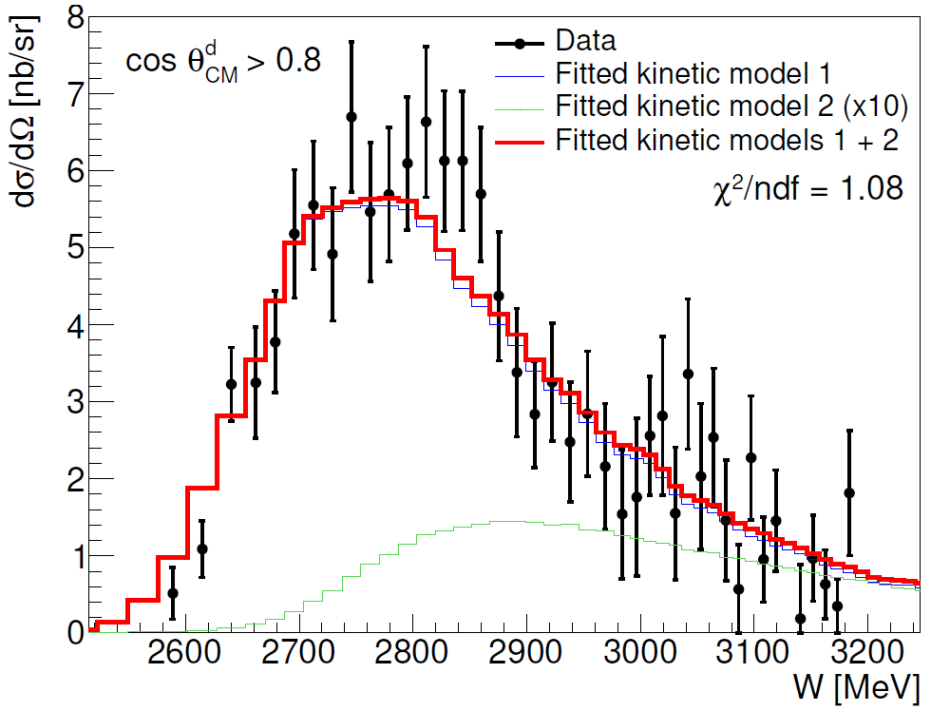

Figure 2.12: Differential cross section for coherent $\gamma d \rightarrow \pi^0 \eta d$ with $\cos\theta^d_{\mathrm{CM}} > 0.8$. Solid lines describe fits of a kinetic model (see reference for further information). Figure taken from [8].

CHAPTER 3

BGOOD experimental setup

The BGOOD experiment was used to collect the data analyzed in this thesis. As such the following chapter describes the setup in greater detail while orienting itself largely on the technical paper [24]. Unless stated otherwise, information is taken from there. Section 3.1 describes the accelerator used to produce the electron beam used by BGOOD which itself is shown in Section 3.2. There are several components of the BGOOD itself but three of them will be described in greater detail since they are relevant to the analysis: the central calorimeter in Section 3.2.2, the forward spectrometer in Section 3.2.3 and the photon flux monitoring in Section 3.2.4.

3.1 The ELSA facility

The ELSA[1] is a 3-stage ring accelerator situated at the Physical Institute of the Rheinische Friedrich-Wilhelms Universität Bonn. It consists of an electron source[2], a linear accelerator LINAC 2[3] which accelerates the electrons up to 26 MeV before they enter the booster synchrotron which can accelerate them up to 1.6 GeV until they are fed into the stretcher ring itself which accelerates them up to a maximum energy of 3.2 GeV. The ring is injected until it is filled with packs of electrons which then can be extracted at the desired energy. Extraction is possible to the hadron physic experiments BGOOD and Crystal Barrel (CBELSA/TAPS) and to the detector test beam line. Fig. 3.1 shows all of the described components and their connections in greater detail.

3.2 The BGOOD experiment

The BGOOD detector was designed to investigate low momentum transfer reactions, which therefore contain very forward going hadrons and residual hadronic systems from the target with low momentum, decaying into almost the full 4π solid angle. To detect particles with both of these kinematics the unique combination of a central detector and a forward spectrometer (FS) was chosen: The central detector encloses the target with a polar angle range of (25–155)° and the FS covers the angular range of (1–12)° in the forward direction. Fig. 3.2 shows the individual detector components and their

[1] Electron Stretcher Accelerator
[2] Either a simple electron gun or a source of spin-polarized electrons, which was not in use during the time of this thesis
[3] LINAC 1 is not in use

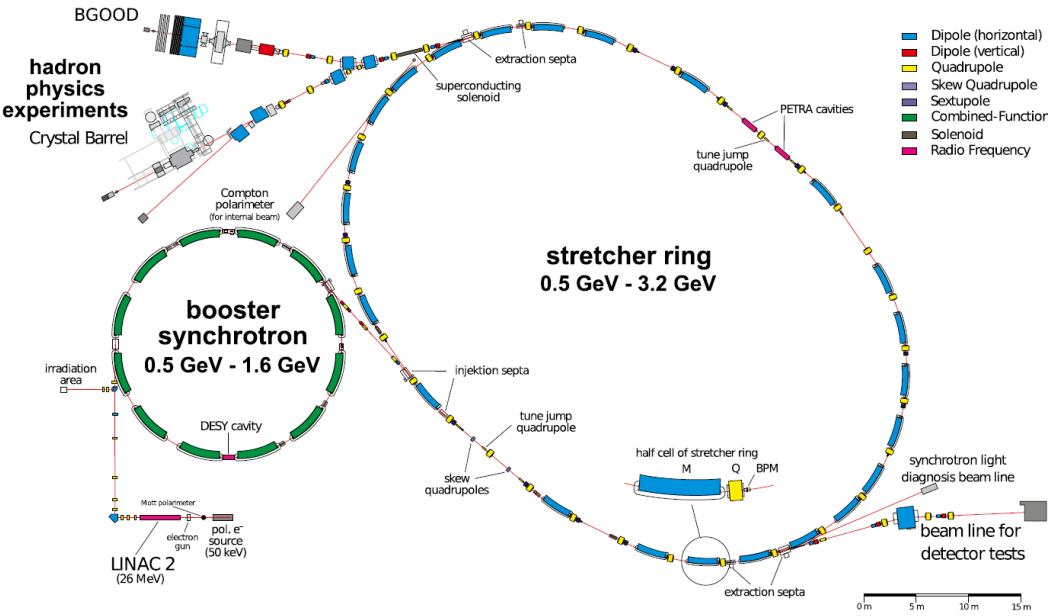

Figure 3.1: Schematic view of the ELSA setup. Figure taken from [24].

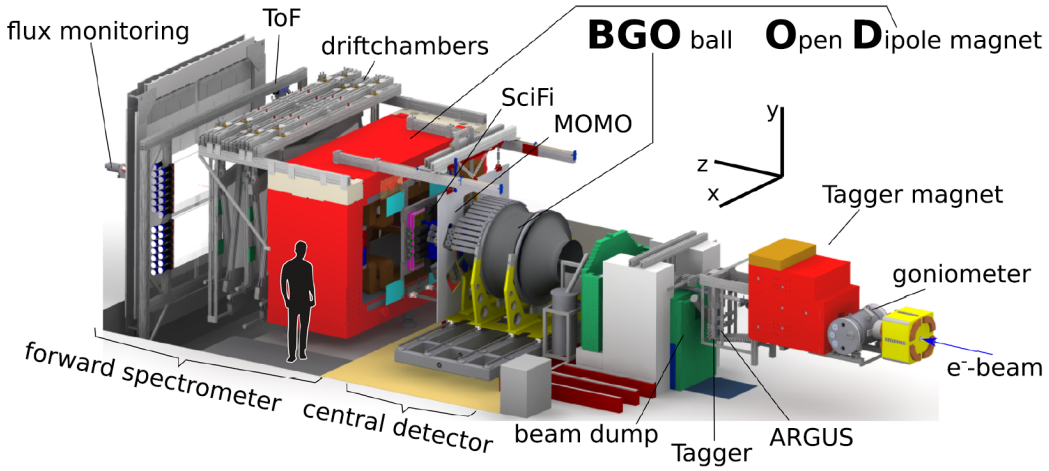

Figure 3.2: Overview over the BGOOD experiment and its components. Figure taken from [24].

arrangement. The production of the photon beam is described in Section 3.2.1 and the central detector is shown in Section 3.2.2 while the FS in Section 3.2.3. Additionally the photon flux is measured by two detectors, the flux monitor (FluMo) and Gamma Intensity Monitor (GIM) which are shown in Section 3.2.4.

3.2.1 Tagger

The tagger converts the electron beam into a photon beam using bremssstrahlung off a radiator. The radiator material has different options, notably copper for incoherent photons and a diamond radiator to produce a polarized beam. The photon beam is then tagged by way of bending the post-bremsstrahlung

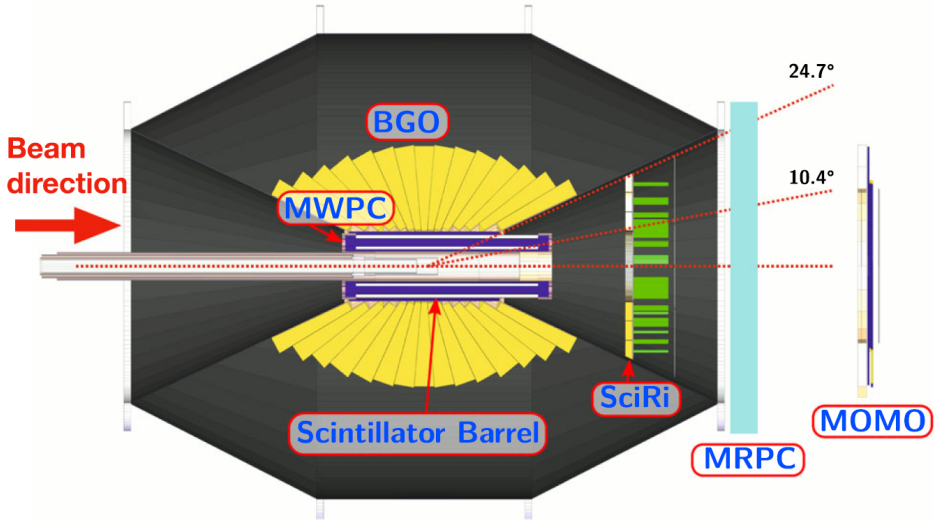

Figure 3.3: Schematic cross section of the central detectors components which are further explained in the text. The MRPC is not in use during the time of this thesis and MOMO belongs to the Forward Spectrometer, see Section 3.2.3. Figure taken from [24].

electrons out of the beamline with a magnetic field and letting them hit a hodoscope. From the electrons' deflection in the field their momentum can be calculated and with it the post-bremsstrahlung energy E'_e. Combining this with the measurements from ELSA which gives the initial electron energy E_e allows for the indirect measurement of the photon beam energy E_γ which enters the central detector housing the target as $E_\gamma = E_e - E'_e$.

ARGUS is an additional scintillating fiber detector which can be used to detect the electrons complementary to the hodoscope. It allows for finer resolution, but was not used in the analysis work of this thesis.

3.2.2 The central detector

Fig. 3.3 shows the parts of the central calorimeter. Furthest inside is the target, a vacuum cryonic cell containing either liquid hydrogen or deuterium. There are two possible sizes of the cell, a short (5 cm) and a long (10 cm) version. When the target is full, the windows at the front and end made out of polyethene terephthalate increase the effective length to 6.1 cm or 11.1 cm respectively. For the work of this thesis data taken from July 2018 with a long deuterium and from November 2018 with a long hydrogen target was used.

Directly around the target two Multi Wire Porportional Chamber (MWPC) are situated. They consist of three separate chambers wound around the previous layer each, insulated from each other by a thin film[4]. The cathode consists of 0.1 µm thick copper strips helically wound with an inclination of $\pm 45^\circ$, while the anodes are gold-plated tungsten wires stretched along the beam axis with a diameter of 20 µm with a distance of 4 mm to the cathodes. A charged particle's impact point can be reconstructed from the intersection of firing anode and cathode wires. Both chambers together then allow for track

[4] Technically 2 films: 2 mm Rohacell covered in 50 µm Kapton

reconstruction[5]. The MWPC covers a polar angular range of (8–163)°.

Between MWPC and BGO there is a barrel of 32 plastic scintillator which are used to later distinguish between neutral and charged particles. For the latter energy loss measurements $\Delta E/\Delta x$ are also provided. This information together with the energy deposited inside the BGO is used for particle identification.

The BGO[6] is the main component of the central detector: A calorimeter consisting of 480 crystals partitioned into 15 *crowns* of 32 crystals each. Fig. 3.3 shows a cross section view where the crowns' arrangement is visible. Each crown covers the full azimuthal ring, corresponding to $\Delta\phi = 11.25^\circ$ per crystal, and a polar angle of $\Delta\theta = (6 - 10)^\circ$. The BGO covers in total the polar angles $(25 - 155)^\circ$. Signals from the crystals are caught and amplified by photomultiplier tubes which are shielded with µ-metal from low magnetic fields while the forward half is protected by an iron shielding against the fringe field of the forward spectrometer's open dipole magnet.

The Scintillator Ring *SciRi* is placed in forward direction to cover the small gap in polar angle acceptance between the BGO and the Forward Spectrometer. Three rings made out of plastic scintillator material are segmented in 32 pieces, achieving an azimuthal angle covered of $\Delta\phi = 11.5^\circ$, same as the BGO rugby ball. Together the three rings cover a polar angle range of $\Delta\theta = (10 - 25)^\circ$, each one 5°. There is a small overlap between the SciRi and the Scintillator Barrel or the MWPC's.

3.2.3 The forward spectrometer

The Forward Spectrometer (FS) is shown in Fig. 3.4 in its components. It is constructed as a magnetic spectrometer and therefore the central part is a large open dipole magnet. It can accept a range of 12.1° in horizontal and 8.2° in vertical direction[7] respective to nominal beam direction. Along the beam axis at maximum current of 1 340 A the integrated field is approximately 0.71 Tm.

Two scintillating fiber detectors, *MOMO* and *SciFi* are placed in front of the magnet to track charged particles. MOMO[8] consists of 672 fibers 5 mm in diameter each. They are partitioned into three layers which are oriented with a 60° angle to the adjacent layer. Each layer consists of two planes of fibers where the fibers of one plane lie in the gaps between the fibers of the other. A central hole 4.5 cm in diameter allow passing the photon beam through. MOMO is used for monitoring the efficiency of other detectors and for track finding. SciFi consists of 640 fibers 3 mm in diameter which form 320 layers with a 90° angle to each other, slightly overlapping. Groups of 16 fibers are connected to a photomultiplier for readout. With µ-metal the photomultipliers are shielded against the magnetic fields from the magnet. In the center there is a 4×4 cm^2 hole to allow the passing through of the photon beam. The SciFi is used for track reconstructing.

Drift chambers behind the dipole magnet perform charged particle tracking in eight double layers. They are oriented perpendicular to the beam axis in 4 different directions: vertical (X), horizontal (Y), +9° against vertical (U) and -9° against vertical (V). The capitals in brackets are the labels used in Fig. 3.4 and together all 8 layers allow for unambiguous track reconstruction. The drift cells have a hexagonal structure and a width of 17 mm with two layers separated 15 mm to resolve left-right ambiguity of the intersections. Anode and cathode wires are made out of gold plated tungsten 25 µm

[5] This is in principle doable, but at the time of this thesis no such reconstructions algorithm to process raw MWPC data existed and therefore MWPC data was not used

[6] An abbreviation for the crystals' material: Bismuth Germanate $Bi_4(GeO_4)_3$

[7] The window is of rectangular shape

[8] Originally built for the Monitor of Mesonic Observables experiment at COSY

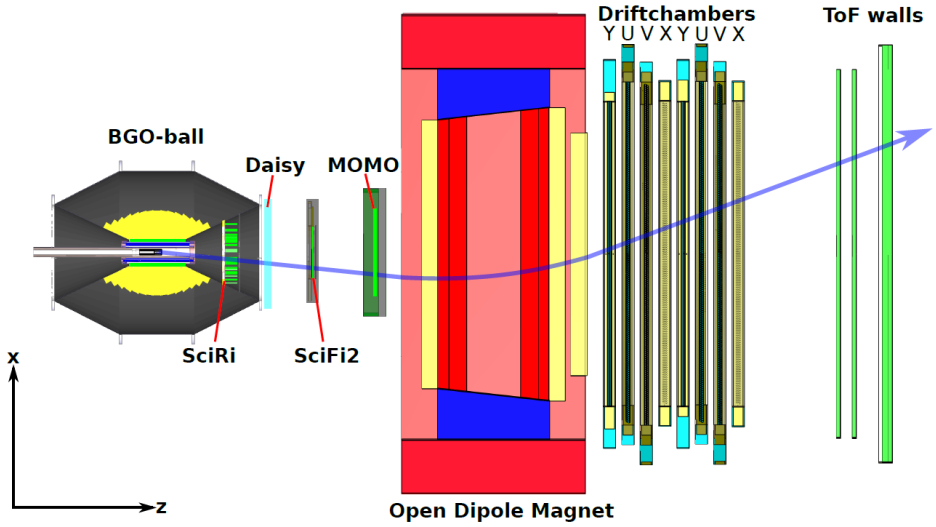

Figure 3.4: Cross Section view of the Forward spectrometer. The BGO-ball and SciRi belong to the central detector, see Section 3.2.2, Daisy is the MRPC previously mentioned (see caption of Fig. 3.3) and the rest are the components of the FS. Figure taken from [25].

in diameter and anodes are set to ground potential, while cathode to around $-2.8\,\mathrm{kV}$. Ensuring field homogenity within the cells and shielding against external fields is done with 200 µm thick gold plated beryllium bronze wires around the drift cells. Since no hole for the photon beam can be made, in the central 5 × 5 cm the anode wires were galvanized with additional gold to increase the diameter to 100 µm which effectively lowers the sensitivity. The gas is 70% Ar and 30% CO_2 which altogether achieves a position resolution $\delta x < 300\,\mu\mathrm{m}$.

Finally the Time-of-flight (ToF) spectrometer is positioned 5.6 m downwards away from the target. It consists of 3 walls made out of scintillator bars with a 10 to 22 cm horizontal gap to let the photon beam and e^- e^+ from pair production in target and air pass. The ToF uses the Time over Threshold (ToT) technique to achieve a time resolution of 0.34 ns when combining the three walls together. This timing information gives when combined with track reconstruction the particle β and together with the momentum from the deflection of charged particles in the magnetic field, which gives the momentum, mass and particle identification can be achieved.

3.2.4 Flux monitor and Gamma intensity monitor

The photon flux can be directly measured by the tagger, however in front of the target two collimator rings are installed to reduce beam halo effects. Thus the effective flux upon the target needs to be determined by a secondary detector which measures the fraction of photons passing the collimators.

At the end of BGOOD's beamline the Flux Monitor (*FluMo*) and Gamma Intensity Monitor (*GIM*) are placed with a distance of 7.2 m and 7.8 m to the target respectively.

The FluMo is a plastic scintillator in five parts, each of which is 5.0 × 5.0 × 0.5 cm in height, width and depth. They are put in series in the beam and detect photons converted into e^- e^+ pairs, which is only a fraction of the bremsstrahlung photons. Therefor the usage requires knowledge about the detection efficiency that is acquired by taking data with a low beam intensity and triggering on the

GIM. Then it can be identified if the FluMo detected such an e^- e^+ pair and the overall detection efficiency of FluMo can be determined.

The GIM is a lead glass detector with full absorption. The photon beam hitting the lead glass undergo electromagnetic showering which are measured by the Cherenkov light they produce. This allows for a high rate stability in comparison the scintillating light but also makes the GIM susceptible to radiation damage and therefore it is not kept in the beam at all times. Instead the FluMo is used to determine the relative photon flux, the GIM is used to calibrate the relative measurement of the FluMo.

Afterwards the photon flux from the tagger can be scaled down depending on the fraction FluMo detects. The flux impeding on the target is a requirement to calculate cross sections and is thus one of the instrumental quantities for this thesis.

CHAPTER 4

Data analysis

The raw data collected by the BGOOD experiment was analyzed in four/five steps to determine the differential/double differential cross section respectively for the coherent $\gamma d \rightarrow \pi^0\pi^0\pi^0 d$ reaction. In Section 4.1 the ExPlORA framework is briefly described, which is used to calculate tracks and events from the raw data provided by the detectors. Simulations were also done with ExPlORA. Secondly various techniques were used to extract the yield out of the whole events, most notably a background subtraction is applied at the end, this is described in Section 4.2. To determine total yield from the observed one, the detection efficiency needs to be determined, which is shown in Section 4.3. Finally Section 4.4 shows the calculation of $\mathrm{d}\sigma/\mathrm{d}\Omega_d$. To further determine the double differential cross section with respect to invariant masses, the pions need to be determined which is described in Section 4.5. Finally this can be used to determine $\mathrm{d}^2\sigma/\mathrm{d}\Omega_d\,\mathrm{d}M_{inv}$, shown in Section 4.6.

4.1 ExPlORA, track and momentum reconstruction

The raw data of the detectors is saved without modifications event-wise on disk. The ExPlORA[1] framework is used to determine usable data by way of forming *tracks* of the particles from detector responses. The specifics of this analysis can be found in the PhD thesis of Oliver Freyermuth [26], here only a general description is given with emphasis on the event reconstruction important to analyzed reaction. The general structure of the analysis are shown in Fig. 4.1. Section 4.1.1 describes ExPlORA details as far as needed, Section 4.1.2 shows the general process of analyzing raw data. Finally, Section 4.1.3 describes a few detail on track reconstruction important for the reaction analyzed in this thesis.

4.1.1 ExPlORA

ExPlORA is the analysis and simulation framework used to analyze raw data from the BGOOD experiment and construct *tracks* based on detector signals. All physics analysis done in this thesis utilizes with ExPlORA reconstructed tracks and simulations to later determine detection efficiencies also utilize the framework. ExPlORA was developed from a fork of the original version, which was utilized by and developed for the CBELSA/TAPS collaboration. It is a C++ extension of CERN's

[1] Extendable Pluggable Objectoriented ROOTified Analysis

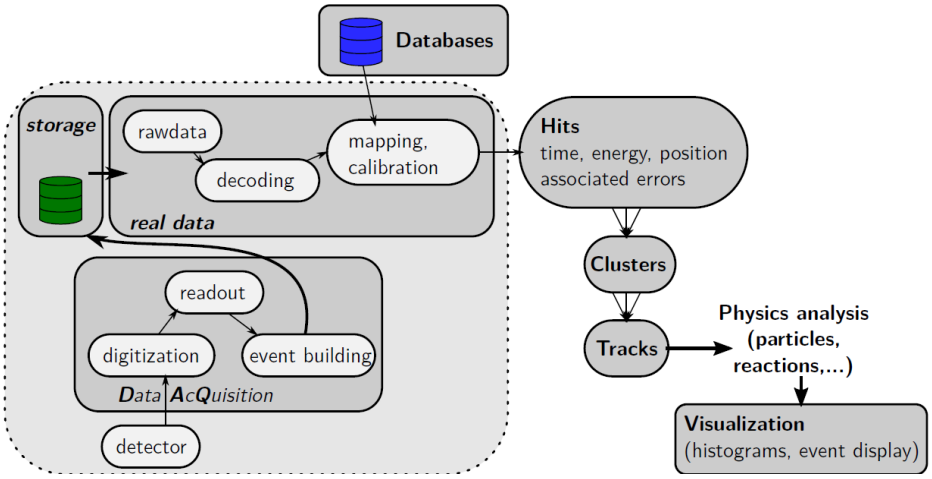

Figure 4.1: Schematic Workflow of the Analysis. Figure taken from [26].

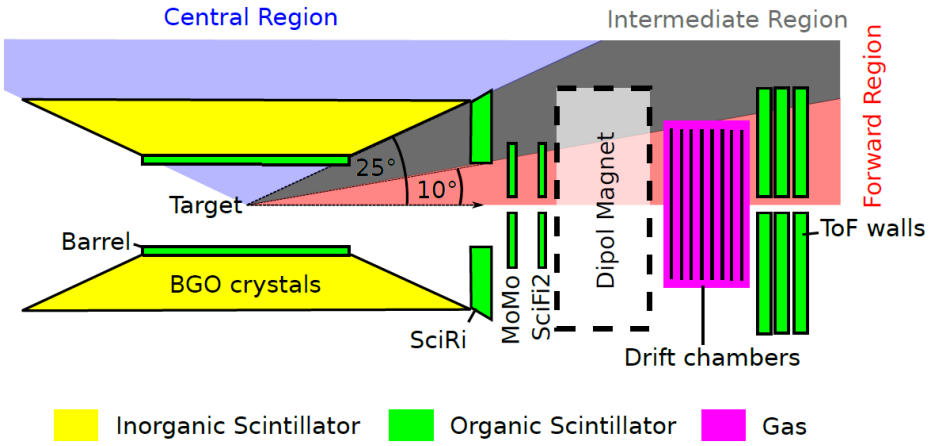

Figure 4.2: Non-scale overview of the polar angle acceptance of the BGOOD detectors. Figure taken from [25].

ROOT library [26] and also contains an implementation of BGOOD's detector geometry and materials, as well as the magnetic fields [25]. The latter is utilized to simulate events in the following procedure:

First the kinematics are determined and the first-generation particles are produced by an event generator. Monte Carlo methods then simulate particle decay and energy disposition by utilizing the stored detector geometry. Geant4[2] is used afterwards to simulate the passage of particles through active detector material [27]. Finally the response is generated which results in an output similar to real data.

4.1.2 Hits, Clusters and Tracks

Post-collision particles are detected by the different detectors depending on their polar angle (see Fig. 4.2) and whether they are charged or neutral. Refer to Chapter 3 for a description of the detectors

[2] Geometry and Tracking 4

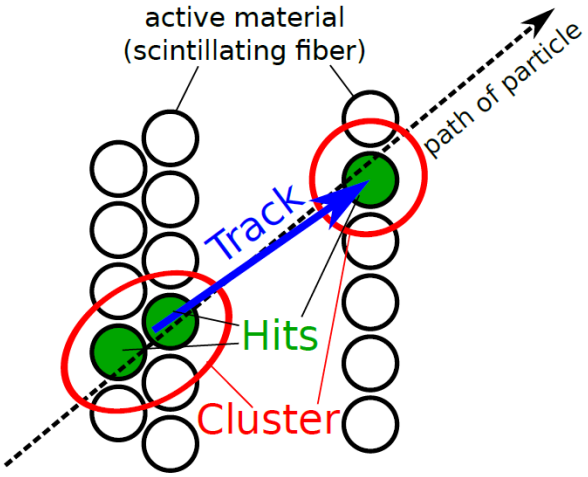

Figure 4.3: Construction of a Track from Clusters and Cluster from Hits. Figure taken from [25].

and their specifics.

A detector responded if the incident particle triggered an electric signal which surpassed a preset threshold. After the detector response has been digitized and events have been built, the raw data is stored as mentioned before. From this point onwards ExPlORA analyzes the data as follows: The raw data is decoded and a database is used to map and calibrate the data, resulting in so-called *hits*. Whenever a particle interacted with a detector part, the corresponding position, time, energy etc. are now stored together with their errors in a bundle, the hit.

The hits belonging to the same incident particle in one detector are then grouped together and form *clusters*. Finally from all detectors the clusters associated with the same particle are combined to a *track*. Fig. 4.3 shows the principle visually. It should be noted that these terms are also used for neutral particles and also in the case that only a single cluster and the (presumed) target origin define a track [26].

Tracks are separated according to acceptance region (central, intermediate and forward) as shown in Fig. 4.2, as well as whether the particle was charged or neutral. Track information can then be exported to a ROOT file containing all particle tracks in the form of 4-vectors (or more accurately `TLorentzVector` objects organized in a `TTree` structure). This thesis used tracks reconstructed from real data and simulated ones, further analyzing them with ROOT scripts.

4.1.3 Track reconstruction in central and forward region

The exact methods utilized by ExPlORA to determine a detected particle's properties and reconstructing the corresponding track differ depending on detector and particle. Here only a few details for the two cases important to this thesis are given: Reconstructing photons in the central detector and charged particles in the forward spectrometer.

Central detector The tracks which are reconstructed in the central region utilize the information from both the BGO and scintillating barrel detector. The latter is used to determine whether a particle was charged or not and in the case of a charged particle further information is utilized to determine the

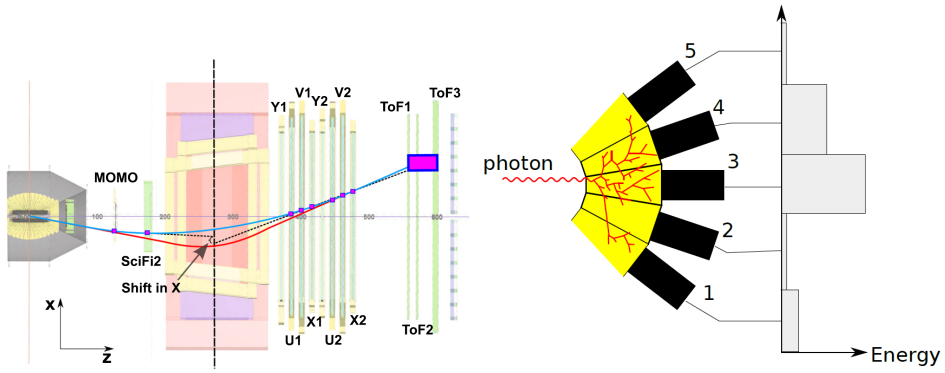

Figure 4.4: Track reconstruction in the Forward Spectrometer (left, [24]) and in the BGO for photons (right, [25]). In the left figure, the dashed lines indicate the track estimation upstream and downstream of the magnet. In red a track estimation made with a box-shaped magnetic field is shown, while in blue a fit after the momentum dependent correction is shown. In the right figure the impact of a photon on BGO crystals is seen while the diagram shows energy disposition in the crystals.

energy deposition in the barrel. For the purpose of this thesis however, only the reconstruction of photons is important.

The BGO is an electromagnetic calorimeter and is optimized for photon and electron detection. Photons undergo electromagnetic showering and the resulting shower spreads to multiple crystals as seen in Fig. 4.4 on the right. The resulting information allows for measuring the photon energy and with knowledge of the crystals scattering length, a weighted average can be made to determine the photons position to greater accuracy than the crystal granularity.

Forward spectrometer For tracks in the forward region, the responses from MOMO, SciFi, the drift chambers and the ToF walls are combined. Before the particle is passing through the magnet, MOMO and SciFi can provide the track, afterwards the drift chambers and ToF walls can provide the necessary information. First the clusters in MOMO and SciFi are combined to form a straight track. Then in the ToF walls and the drift chambers are checked for matching clusters which are then combined to form another straight track. These are shown in Fig. 4.4 on the left as two dashed lines. Due to fringe fields and non-uniformities of the magnetic field, both tracks have a slight shift in x-direction in the magnets center. With approximating the field as a uniform box-shaped field, a track can be made, shown in Fig. 4.4 on the left as a red line. At this point, a first momentum p estimation can already be made. This combined with the time of flight determined by the ToF walls which give the particle velocity β, is used to estimate the particle's mass (see Eq. (4.1)) and to make a hypothesis on the type of particle measured.

$$m = \sqrt{p^2 \left(\frac{1}{\beta^2} - 1 \right)} \tag{4.1}$$

After taking into account the energy losses depending on the type of particle measured (e.g. proton, kaon, deuteron) a fit is made which has the best agreement between detector information and fitted track. This fit is shown in blue in Fig. 4.4, left.

In Fig. 4.5 particles' reconstructed momentum and velocity in the forward spectrometer can be seen.

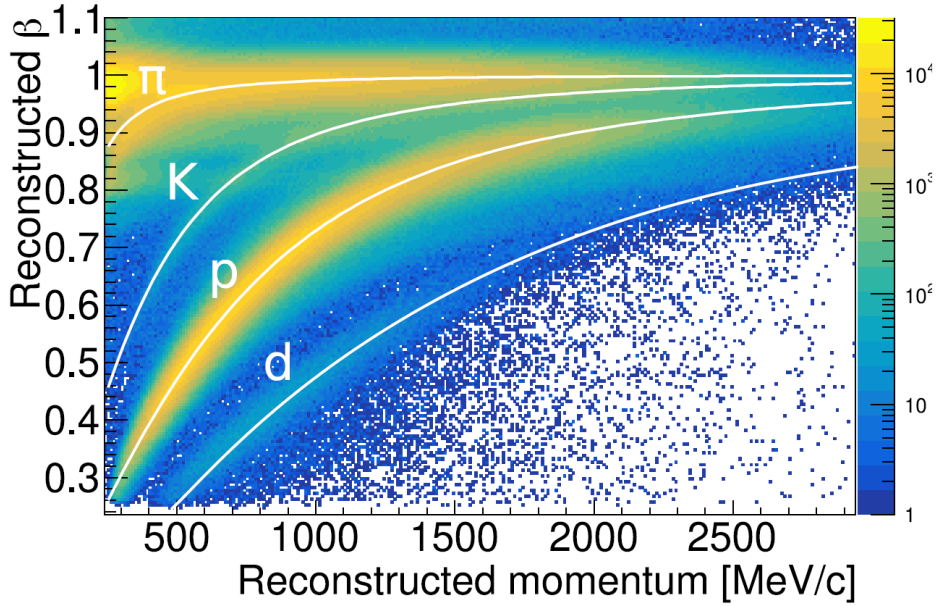

Figure 4.5: Reconstructed particle velocity β versus momentum in the forward spectrometer. The solid white lines show β depending on momentum and indicated particle mass. Figure adapted from [24].

Clearly visible are the correlations, and for several particles the functional dependency according to Eq. (4.1) is depicted, where the nominal mass has been used to determine the white solid lines. As can be seen, the forward spectrometer is clearly able to distinguish between deuterons and protons on a momentum scale of 500 MeV to 2 000 MeV. This is already surprising considering that the deuteron momentum in this case can surpass its fermi momentum by a factor of around 10.

4.2 Yield extraction and background subtraction

The real data sample utilized in this thesis was taken in July 2018 with a deuterium target. In the first step ExPlORA is utilized and the tracks are exported and saved in a separate ROOT file as mentioned before. The ROOT file contains each track in 4-vector form, which are organized in a ROOT-specific structure.

When exporting the events several requirements were already made to ensure efficient further processing of data. Each event was required to have

- 6 uncharged and no charged tracks in the central region
- 0 tracks in the intermediate region
- 1 positively charged and no uncharged tracks in the forward region

This resulted in a total of 240 509 events selected. The reason for these requirements is that the goal is to measure the differential cross section at deuteron angles $\cos\theta^{d}_{CM} > 0.8$ (the CM stands for center-of-mass frame, where the deuteron angle is measured). Therefore the deuteron needs to be measured in the forward region. Since the neutral pions are more than 10 times lighter in mass than

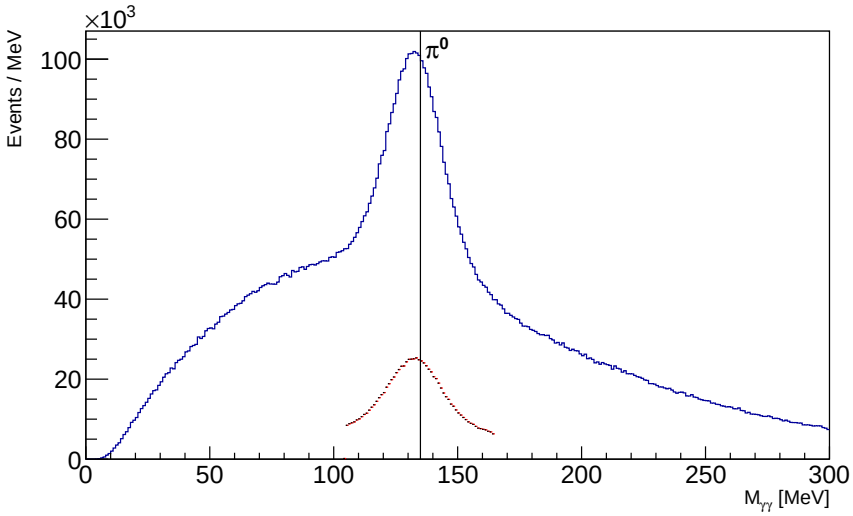

Figure 4.6: Invariant mass of two photons before (blue) and after (red) the mass cut. In black the nominal π^0 mass is marked.

the deuteron, the angular spread of the pions is expected to be larger. Also, with their mean life they can travel about $c\tau = 25.5\,\text{nm}$ [10], which means they will decay inside the BGO ball. Since the main π^0 decay $\pi^0 \rightarrow \gamma\gamma$ has a branching ratio of 98.8% [10], the 3 π^0's decay into 6 photons in 96.5% of all cases. These 6 photons should then be detected in the BGO. No other tracks are produced by the reaction and therefore exclusivity is demanded.

From this point on ROOT scripts in C++ are utilized all of which are created by the author of this thesis unless otherwise stated.

4.2.1 Pion mass cut

First it is determined whether or not the 6 measured photons can be reconstructed to 3 neutral pions. For that it is important to keep the reaction's multiplicity in mind: Following this the way photons are arranged into pairs, where each pair represents a pion decay, is called a photon combination. The total number of these combinations is determined by counting the possible permutations of photons and dividing by the number of permutations which can't be distinguished in the experiment. Since π^0's cannot distinguished from each other, a factor of 6 must be divided out. The 2 photons from each decay can also be switched with each other and this gives a factor of 2^3. This makes for a total of

$$\frac{6!}{6 \cdot 2^3} = 15 \tag{4.2}$$

different permutations.

A priori the correct photon combination is of course not known, or even if such a combination exists. Thus all 15 combinations are made and then the invariant mass of the photon pairs is checked. If all three invariant masses for a combination lie within ±30 MeV of the nominal π^0 mass, the combination is saved.

The histogram in Fig. 4.6 shows the result of this cut. In blue the invariant masses of all photon

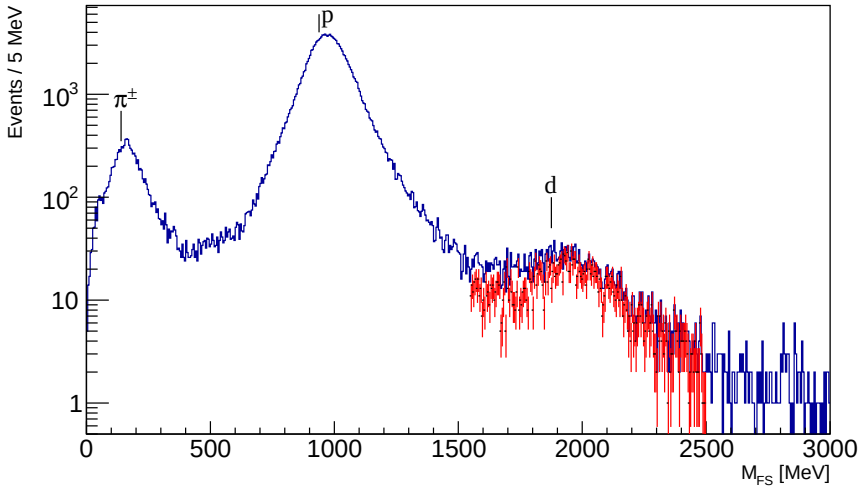

Figure 4.7: Mass of the particle in the forward spectrometer before (blue) and after (red) deuteron mass cut. Note that y-scale is logarithmic. Various nominal masses of particles are marked at peaks.

pairs of all combinations and events can be seen. In red only the invariant masses of the photon pairs in the combinations which pass the mass cut can be seen. For this reason the height of the histogram is different before and after the cut. The black line marks the nominal π^0 mass at 134.98 MeV [10]. The invariant masses don't peak exactly at the π^0 mass because they are measured in the BGO, which is not exactly calibrated to the π^0 mass and has a small deviation.

4.2.2 Deuteron mass cut

Next the positive charged track's mass in the forward spectrometer is checked. If the particle's mass was within 1 550 to 2 500 MeV it was saved as a deuteron. The reason for this asymmetric cut can be seen in Fig. 4.7:

The figure shows the charged particle's mass in the forward spectrometer before the cut in blue. The three peaks mainly seen are marked with nominal particle masses. The lowest lying peak belongs to π^+'s which are produced in the collision and can survive long enough to be detected in the forward spectrometer. The proton peak comes from deuteron break-ups which also has the greatest height. The highest mass peak is the deuteron one, which is also the lowest recognizable one.

The lower end of the deuteron mass peak merges with the proton mass peak, which is why the cut is tighter there to avoid background from protons. On the higher mass end this does of course not occur so the cut can be more relaxed. The red data points are the events which fall in this mass cut while also requiring to have at least one photon combination saved before. For this reason the red points don't overlap with the blue line completely.

For all events in which the charged particle falls in the mass cut it is saved as a deuteron for later use.

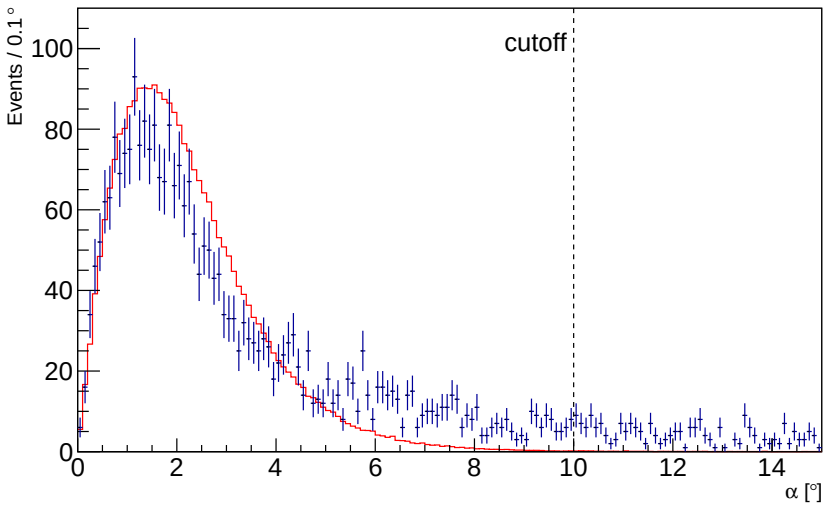

Figure 4.8: Angle between reconstructed (see text) and measured 4-momentum in the forward spectrometer. In red the simulated events scaled down to match the data points in blue

4.2.3 Momentum conservation cut

From this point on it is implied that an event satisfies the previous cuts, e.g. here that the events have at least one valid photon combination and a deuteron saved.

According to momentum conservation, the 4-momentum p of the particle in the forward spectrometer is determined as

$$p'_d = p_d + p_\gamma - p_{\pi^0,1} - p_{\pi^0,2} - p_{\pi^0,3} \text{ where } \quad p_{\pi^0,i} = p^i_{\gamma,1} + p^i_{\gamma,2} \tag{4.3}$$

Here p'_d is the 4-momentum of the particle in the forward spectrometer, ideally the deuteron post-collision. p_γ is the 4-momentum of the beam and $p_{\pi^0,i}$ of the i-th pion. $p^i_{\gamma,1}$ and $p^i_{\gamma,2}$ correspond to the 4-momenta of the two photons decayed from the i-th pion. Since the target is cooled, the deuterons are taken at rest before collision. Thus the 4-momentum of the target is set to

$$p_d = (m_d, 0, 0, 0) \tag{4.4}$$

With this the measured 4-momenta can used to calculate the 4-momentum of the forward spectrometer particle p^{rec}_d with Eq. (4.3). This can be then compared to the measured 4-momentum p^{meas}_d. For that the angle α between both vectors is calculated

$$\alpha = \angle(p^{rec}_d, p^{meas}_d) \tag{4.5}$$

This angle is then plotted for both real data and a simulation of the coherent $\gamma d \to \pi^0\pi^0\pi^0 d$ created with ExPlORA. The same analysis as before is done in the simulated data and the same histogram is created. Fig. 4.8 shows both in comparison, where the simulated events have been scaled down for visibility. The simulation shows that for no event α should be greater than 10° since the detector resolution is expected to be good enough to determine p'_d to this accuracy. So a cut is made

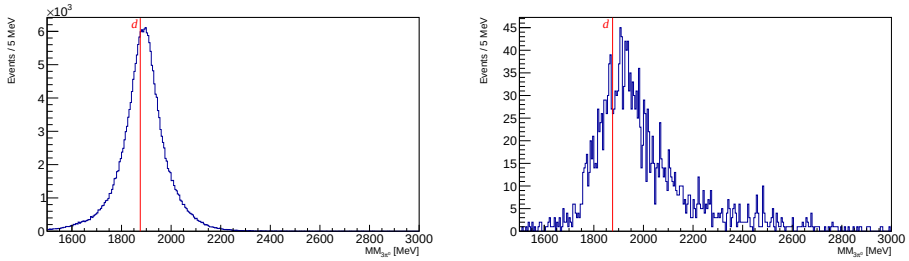

Figure 4.9: Histogram of the missing mass to 3 π^0. On the left simulated events are depicted and on the right real data together with a red line marking the nominal deuteron mass.

on data, requiring $\alpha < 10°$, which can also be seen in Fig. 4.8. This cut is not optimized, as it could be made tighter to remove more background while also cutting into the signal as long as the signal-to-background ratio would become better than before. The choice of 10° is simply the point at which only background remains which may safely be cut away.

4.2.4 Forward deuteron angle cut

The last cut is made on the polar angle of the deuteron. For that the 4-momentum of the particle in the forward spectrometer is boosted to the center-of-mass frame by boosting it with $p_\gamma + p_d$ (beam and target 4-momenta). Then the cut is made such that only events with $\cos\theta^d_{CM} > 0.8$ remain.

At this point various histograms are made, most importantly E_γ versus $\cos\theta^d_{CM}$ and E_γ vs. the missing mass to $3\pi^0$ (see Section 4.2.5 for details).

4.2.5 Background subtraction

After all cuts are made the so-called missing mass to $3\pi^0$ is checked. This missing mass is defined as the invariant mass of Eq. (4.3), so the "mass missing from the total if the three pions are subtracted". A comparison between simulated events and data can be seen in Fig. 4.9. Compared to the simulated events on the left, real data shows a clear shoulder at higher masses.

This shows that even after the deuteron mass cut in Section 4.2.2 some events with quasi-free[3] production off a proton still remain. These are removed by subtracting this quasi-free background.

For this the same analysis as detailed above is done on data taken in November 2018 where the target was filled with cooled hydrogen. In this way only protons remain as target particles and the analysis results in background events[4]. The resulting histograms are then scaled by photon flux up to the flux of the original data:

$$N_Y(E_\gamma) = N_Y^{sig}(E_\gamma) - \frac{N_\gamma^{sig}(E_\gamma)}{N_\gamma^{back}(E_\gamma)} N_Y^{back}(E_\gamma) \tag{4.6}$$

N_Y is here the yield after background subtraction, N_Y^{sig}, N_Y^{back} the histogram entries from the signal

[3] Called this because the proton originates from the break-up of a deuteron and is still influenced by the fermi momentum of the nucleus

[4] Since the deuteron is bound only shallowly the fermi momentum can be neglected in this case

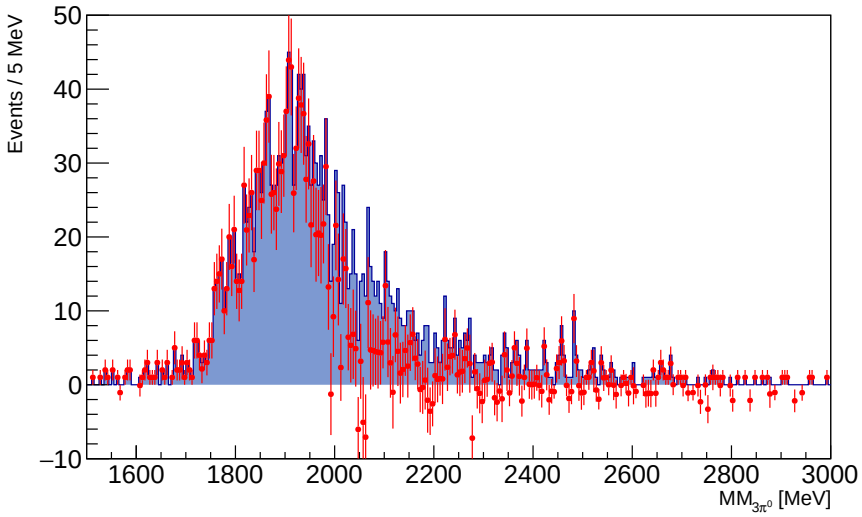

Figure 4.10: Missing mass to $3\pi^0$ before (shaded blue) and after (red data points) background subtraction.

and background data respectively and N_γ^{sig}, N_γ^{back} the photon flux values for signal and background data respectively. The results from the deuteron target data are here called "signal" data and the one from hydrogen target data "background" data.

The effect of this background subtraction can be seen in Fig. 4.10. Compared to before, the red data points show that the higher missing mass shoulder is now more symmetrical to the lower one, and after a certain point data is mostly consistent with zero entries. Some data points seem to be below zero even after taking statistical error into account, but this can be explained by further adding systematical error. In Section 4.4.1 this will be detailed, but an error of 9.3% needs to be added on top of the statistical one[5]. With this, all data points are consistent to be greater or equal zero.

After this background subtraction, the 2-dimensional histogram which shows events partitioned in beam energy E_γ and deuteron angle $\cos\theta_{CM}^d$ is used to extract the reaction's yield in dependence of beam energy.

4.3 Detection efficiency calculation

To calculate the differential cross section, it is mandatory to know the detection efficiency of the experimental setup and analysis procedure. This is calculated by using simulated data, for which the "true" kinematic event distribution is known. After the analysis procedure is used on the simulated output, the comparison between yield from analysis and "true" yield results in the detection efficiency. Since the simulation includes energy losses in detector material and detector response, the efficiency of both hard- and software can be calculated.

[5] Strictly speaking this is the error on the differential cross section, but it should be a good approximation

4.3.1 ExPlORA simulated dataset

The data set used to extract the detection efficiency was simulated using ExPlORA, see Section 4.1.1. The $\gamma d \rightarrow \pi^0\pi^0\pi^0 d$ reaction was given to be generated and the detector response was simulated by ExPlORA. A total of 40 million events were generated this way. The resulting ROOT file contains both the generated deuteron and photon beam 4-momenta, as well as the simulated output that is modeled after real data results.

4.3.2 Yield extraction with analysis

The yield needs to be extracted with the same cuts and procedures as the real data before to make the software efficiency accurate. However there are two small points that need to be adjusted for the simulated events.

1. Since only the first generation particles are predetermined and their decays are Monte-Carlo simulated, the $\pi^0 \rightarrow \gamma\gamma$ decay is not ensured. This means that at the beginning of yield extraction with the ROOT script, 6 neutral tracks in the central region must be required to ensure the same conditions as for real data.

2. Since only coherent events are generated, no background subtraction is needed.

With these adjustments, the yield can be extracted from the same histogram as for the real data.

4.3.3 True Yield extraction

The "true" yield is determined from the generated particles, which were saved from each event. No further selection except ensuring that the deuteron angle fulfills $\cos\theta^d_{CM} > 0.8$ is needed since only relevant events were generated. The 2-dimensional histogram of deuteron angle versus beam energy is filled with the generated track data (e.g. by tacking the energy of the generated tagger photon and polar angle of the generated post-collision deuteron). Then the "true" yield in dependence of the beam energy can be extracted (by integrating over all polar deuteron angles $\cos\theta^d_{CM} > 0.8$).

4.3.4 Calculation

To determine the detection efficiency after both yields have been counted is as simple as dividing them:

$$\epsilon(E_\gamma) = \frac{N_Y(E_\gamma)}{N_Y^{true}(E_\gamma)} \tag{4.7}$$

Here N_Y is the yield from the analysis and N_Y^{true} is the "true" yield from generated tracks. ϵ is the detection efficiency. Fig. 4.11 shows the calculation's result. Between 500 MeV and roughly 1 000 MeV the efficiency rises from less than 0.2% to about 8%. Afterwards it experiences a nearly linear drop to about 5% at 2 500 MeV.

This behavior falls within expectations since at lower energy the reaction is only slightly above threshold and is thus kinematic constrained. Here only small amounts of energy can be transferred to the produced pions and they are less likely to be detected. This can be due to photons leaving the BGO, which is more likely since the pions have less energy transferred to them and are more likely to

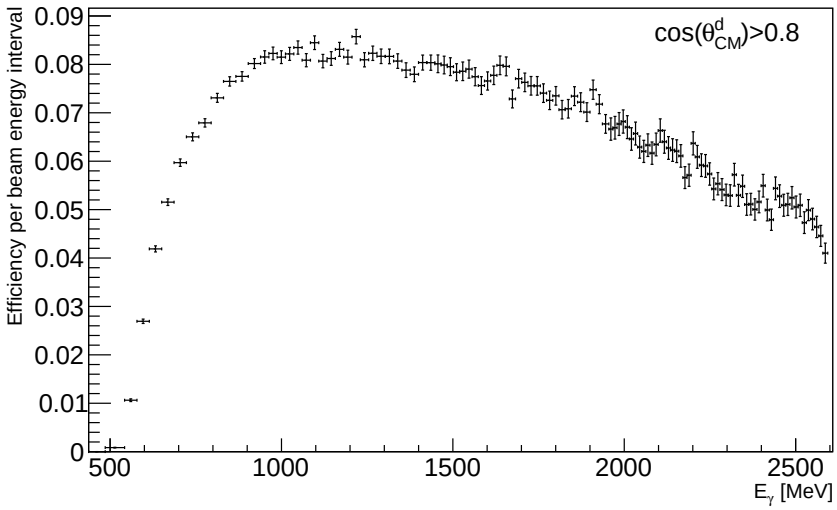

Figure 4.11: The detection efficiency of the analysis depending on beam energy.

travel in forward directions. But it is also possible that the photons decaying from the low-energy pions don't surpass the hardware trigger thresholds and aren't detected. Another possibility is that the deuterons don't get enough energy transferred to be detected inside the forward spectrometer due to insufficient velocity. All of these possibilities become less likely the more center-of-mass energy W is available, which is why with rising beam energy the detection efficiency begins to rise.

After a certain point is reached the detection efficiency begins to fall since another effect dominates: The deuterons are more likely to break up the more energy is transferred to them. It is indeed surprising that at beam energies surpassing the deuteron's binding energy by 100 – 1000 times we can even observe them. But nonetheless this makes it of course difficult to reconstruct the reaction at higher beam energies and leads to a dropping efficiency.

4.4 Differential cross section

The differential cross section is calculated according to

$$\frac{\mathrm{d}\sigma}{\mathrm{d}\Omega_d}(E_\gamma) = \frac{N_Y(E_\gamma)}{N_\gamma(E_\gamma) \cdot \epsilon(E_\gamma) \cdot A_t \cdot \mathrm{d}\Omega_d} \tag{4.8}$$

where
N_Y: Yield from analysis
N_γ: Photon flux
ϵ: Detection efficiency
A_t: Target area
$\mathrm{d}\Omega_d$: Covered deuteron solid angle

Two quantities, the yield and detection efficiency where already determined in section Section 4.2

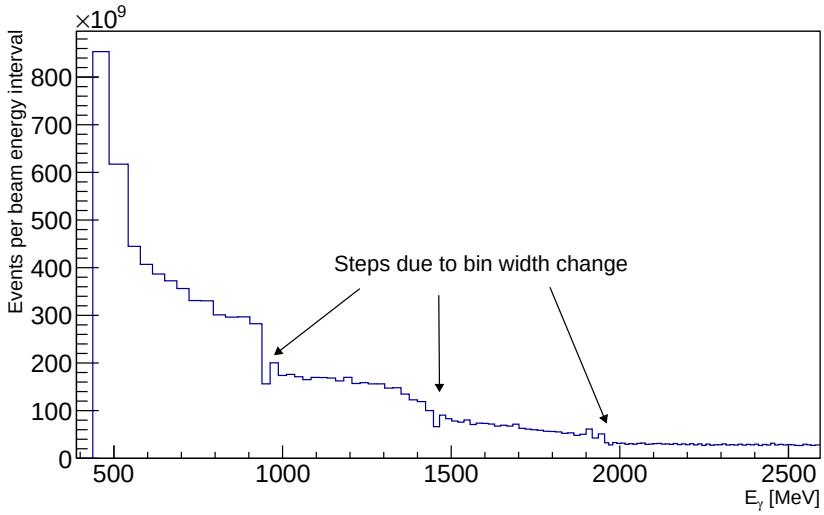

Figure 4.12: The photon flux of the July 2018 data set.

and Section 4.3 respectively. The photon flux N_γ is measured by the experimental setup (see Section 3.2.4) and can be used as-is.

Fig. 4.12 shows this measured flux. The general shape is the typical bremsstrahlung distribution, but there are 3 "steps" where this is broken. The reason is that the tagger hodoscope changes at these points in width and the resulting bin width of the beam energy also changes. All histograms who have an axis depicting beam energy have the same bin width distribution.

The target area A_t is determined by the density of deuterons inside the target and the effective target length. The density of deuterons inside liquid deuterium is $5.053 \times 10^{-8}\,\mu b^{-1} cm^{-1}$ [25] and the effective target length for the long target utilized for this data set is 11.1 cm [25]. This results in an target area of $A_t = 5.609 \times 10^{-7}\,\mu b^{-1}$.

The covered deuteron solid angle is determined by integrating over the θ and ϕ angles:

$$d\Omega_d = \int_0^{2\pi} \int_{0.8}^{1} d\cos\theta\, d\phi = 0.4\pi \tag{4.9}$$

With this the differential cross section $d\sigma / d\Omega_d$ is calculated. See Section 5.1 for the results and discussion.

4.4.1 Systematical errors

Lastly the accompanying systematic errors need to be calculated. There are multiple sources like hardware uncertainties and software modeling but a good part of these has already been calculated for previous works. Most systematic errors are taken from [28] (see Table 4.1) but two exceptions need to be made: When cuts are made on the invariant mass of two photons or on the deuteron mass, there is an error made when the simulation does not match the data in distribution width. When this happens, the simulation will have smaller or wider cuts than the data, influencing the detection efficiency. This results in a systematic error which can be quantified by tightening/widening the cuts and testing their

Error source	% Error
π^0 selection	5.3
Beam spot alignment	4.0
Photon flux	4.0
SciFi efficiency	3.0
Target wall contribution	2.0
Track time selection	2.0
Target length	1.7
ToF wall efficiency	1.5
MOMO efficiency	1.0
Drift chamber efficiency	1.0
Beam energy calibration	1.0
Modelling of hardware triggers	1.0
d selection	1.0
Summed in quadrature	9.3

Table 4.1: Systematic errors on the cross section calculation. Mostly taken from [28], d and π^0 identification after [7].

influence on the cross section.

This was made for the $\gamma d \rightarrow \pi^0\pi^0\pi^0 d$ reaction and since the cuts made on d and π^0 mass were the same as in this thesis, the systematic error on d resolution of 1% was taken from there (see [7]). For the pions, a scaling was applied to the error from [7] to account for the additional π^0 present in the reaction analyzed in this work. Since the cut is made on *all* pions (see Section 4.2.1) the error scales with particle count. This results in an error of 5.3%.

All errors are summed in quadrature (the square root was taken over the sum of the squares of individual errors), resulting in a total error of 9.3% which needs to be applied to the differential cross section. It is shown alongside the results in Section 5.1.

4.5 Pion identification

There are 4 invariant masses whose distribution can be calculated: The invariant masses of $2\pi^0$, $3\pi^0$, $\pi^0 d$ and $\pi^0\pi^0 d$. To calculate these, the individual pions need to be reconstructed. This is not needed for the differential cross section $\mathrm{d}\sigma/\mathrm{d}\Omega_d$ since all cuts and calculations only involve the sum of all pions 4-momenta, which translates to the sum over all 6 photons' 4-momenta.

4.5.1 Reconstruction

To reconstruct the individual pions an algorithm is applied after all cuts have been made, but before the background is subtracted:

For each saved pion combination (e.g. combinations which passed the mass cut) the value

$$\delta m^2 = \sum_{i=1}^{3} (m^i_{\gamma\gamma} - m_{\pi^0})^2 \tag{4.10}$$

Bins summed	W energy range [MeV]
9 – 19	2 413–2 687
20 – 29	2 687–2 852
30 – 40	2 852–3 014
41 – 70	3 014–3 321

Table 4.2: Binning of the invariant mass distribution in W together with the corresponding bins of beam energy which were summed up.

is calculated. Here $m^i_{\gamma\gamma}$ is the invariant mass of the two photons who decayed from the i-th pion in this pion combination. m^0_π is the nominal pion mass. This δm^2 represents how close to the nominal pion mass the three π^0's are in this specific reconstruction.

After this value has been calculated for all saved pion combinations, the combination for which δm^2 is minimal is used to reconstruct the pions. Once the pion 4-momenta have been reconstructed, their mass is set to the nominal pion mass by adjusting the absolute momentum:

$$|\vec{p}| = \sqrt{E^2 - m^2_{\pi^0}} \tag{4.11}$$

This can be done due to the fact that the 4-momentum is reconstructed from the photons measured in the BGO. This means that the pions' energy can be measured, but the mass depends on the angle between the decay photons. This in turn means that this mass can be adjusted within angular resolution limits (for the resolution of the BGO crystals see Section 3.2.2). The adjusted 4-momenta of the pions are then saved.

These are used to built histograms of beam energy versus the invariant mass of $2\pi^0$, $3\pi^0$, $\pi^0 d$ or $\pi^0\pi^0 d$ are built. It is to be noted that the invariant masses of $\pi^0\pi^0$, $\pi^0 d$ and $\pi^0\pi^0 d$ are filled 3 times per event, since any single choice of one or two pions would be arbitrary.

These histograms are then background corrected in the same way as before (see Section 4.2.5). This way the yield for the invariant mass distributions can be calculated. By integrating over beam energy 4 bins are made corresponding to 4 bins of center-of-mass energy W. The range of these bins is shown in Table 4.2 together with the bins which were summed over in beam energy. The highest energy bin is made bigger purposefully since data is more sparse in this region and a higher statistical precision can be achieved this way.

4.5.2 Detection efficiency

The detection efficiency for the invariant mass distributions is calculated the same way as the one for the differential cross section (see Section 4.3) with the exception that different histograms are built, beam energy versus the invariant mass for each different invariant mass. For this the 4-momenta of the generated pions need to be saved in the ROOT file, since they are needed to built the "true yield" histograms. Since the simulation, as explained in Section 4.3, generates decays with MC methods, here the $\pi^0 \to \gamma\gamma$ decay is also not guaranteed. Because of this the ROOT script needs to ensure that from each pion only 2 particles decay in order to compare the simulations to real data correctly.

From these histograms the same 4 bins in beam energy as for the yields before are projected out for all 4 invariant masses. Dividing the number of events yielded by the analysis with the number of

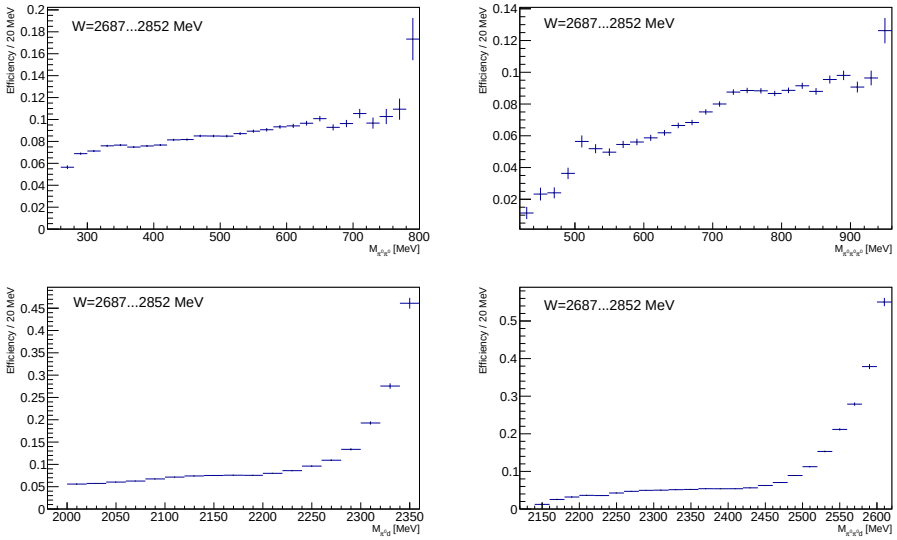

Figure 4.13: Detection efficiencies depending on the various invariant masses: Top left $2\pi^0$, top right $3\pi^0$, bottom left $\pi^0 d$ and bottom right $\pi^0\pi^0 d$.

events generated results as before in the detection efficiency, only now depending on the corresponding invariant mass and separated into 4 energy bins.

The Fig. 4.13 shows examples for the calculated detection efficiencies depending on one of the 4 invariant masses in the center-of-mass energy bin $W = 2\,687 - 2\,852$MeV. The efficiencies are mostly flat, at the edges there is a rise with higher invariant masses visible, but this effect has also bigger statistic uncertainties. This originates from the fact that fewer events are available in simulation here. The effect of this behavior on the invariant mass distributions is limited however, as almost no events fall in this edge regions. In Appendix A all detection efficiencies for all invariant masses and all energy bins are listed.

4.5.3 Systematic error on pion reconstruction

The algorithm described in Section 4.5.1 to reconstruct the individual pions is of course not guaranteed to give back the "true" reconstruction of pions. To analyze the probability of failure, a simulation was made with a ROOT script[6]. The reason for not using a full ExPlORA simulation, which would also include detector effects, is that the simulation output can give out the generated tracks and the simulated detector output, but to the current knowledge of the author it is not possible to connect both. I.e. the simulated measurement cannot be sorted to each generated track with 100% accuracy which defeats the purpose of simulating the measurement in the first place. This of course means, that the following simulation can only give an estimate of the error made, since detector resolution effects are certain to increase the error, but it is a good first estimate.

The simulation generated coherent $\gamma d \rightarrow \pi^0\pi^0\pi^0 d$ reactions and the $\pi^0 \rightarrow \gamma\gamma$ decays. Photons from these decays were then smeared in energy and angle by simulating the detector resolution. This was done by randomly sampling from a distribution around the generated value. For the energy, this

[6] This script was based upon a script by T. Jude and modified by the author of this thesis for the purpose described.

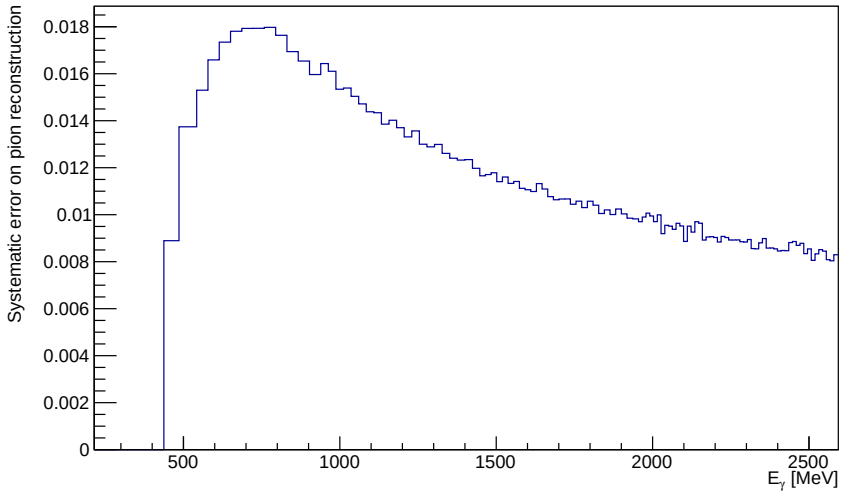

Figure 4.14: The systematic error made by the pion reconstruction depending on beam energy E_γ.

was a gaussian centered around the generated value E with a width of $0.0127 \cdot E$. For he polar and azimuthal angles a uniform distribution was used. For the polar angle θ this distribution had a width of $\pm 5^\circ$ around the generated value and for the azimuthal angle ϕ the width was $\pm 7^\circ$. These values for the BGO resolution were taken from [24].

Afterwards δm^2 was calculated for all pion combinations from these smeared photons and it was counted how often the algorithm selected the wrong combination. Histograms with the same binning in W and m as for the invariant masses were made and the systematic error was calculated by dividing the number of wrong selections by the total events generated. Overall 50 million events were generated.

Fig. 4.14 shows the result, the systematic error depending on beam energy E_γ (the separate calculations for each invariant mass and W bin are not shown for readability). After threshold, the error rises fast to about 1.8% and drops slowly afterwards with higher energy to about 0.85%. Altogether the error is rather unexpectedly small but no simple reason for this can be discerned.

This error is added together with the 9.3% from other sources (see Section 4.4.1) in quadrature for the invariant mass distributions.

4.6 Differential cross section with respect to invariant masses

To investigate the invariant mass distributions, the double differential cross section $\mathrm{d}^2\sigma / \mathrm{d}\Omega_d \, \mathrm{d}m_{inv}$ is calculated for each different invariant mass m_{inv}. The calculation is done with the equation

$$\frac{\mathrm{d}^2\sigma}{\mathrm{d}\Omega_d \, \mathrm{d}m_{inv}}(E_\gamma, m_{inv}) = \frac{N_Y(E_\gamma, m_{inv})}{N_\gamma(E_\gamma) \cdot \epsilon(E_\gamma, m_{inv}) \cdot A_t \cdot \mathrm{d}\Omega_d \cdot \mathrm{d}m_{inv}} \tag{4.12}$$

The notation is the same as before with the addition of the quantity $\mathrm{d}m_{inv}$ which is the bin width of the invariant mass axis. Here $\mathrm{d}m_{inv} = 20\,\mathrm{MeV}$. A further notable difference is that yield and efficiency are now dependent on the invariant masses. Section 4.5.1 and Section 4.5.2 showed how this dependency

was introduced in the calculation. Care must be taken to ensure that detection efficiency and yield are calculated separately for each bin in W before dividing. The photon flux must be integrated over the interval in E_γ corresponding to the bin in W which is calculated. The other constants A_t and $\mathrm{d}\Omega_d$ are the same as before.

With this the invariant mass distributions can be calculated, see Section 4.6 for the results and discussion.

4.6.1 Phase space simulation

The invariant mass distribution is compared to a simulation of pure phase space. This is done with a ROOT script[7]. 100 million events for $\gamma d \rightarrow \pi^0\pi^0\pi^0 d$ are generated and filled in histograms with the same binning in invariant mass and W as the invariant mass distributions. Here again the histograms with one or two pions in the invariant mass are filled 3 times because of the ambiguity in choosing the pions.

To match the invariant mass distributions, the phase space histograms are scaled down, so that the integrals between the two match inside the diagram where they are compared (e.g. for each bin in W and different invariant mass). The comparison between pure phase space and measured invariant mass distribution is shown in Section 5.2.

[7] Based upon a script by T. Jude and modified for the coherent $\gamma d \rightarrow \pi^0\pi^0\pi^0 d$ reaction by the author

CHAPTER 5

Discussion of results

5.1 Differential cross section and comparison to other works

The measured cross section together with the systematical error is shown in dependence of beam energy in Fig. 5.1. The cross section shows a rise to about 7 nb/sr followed by a drop until a beam energy of around 1 500 MeV where a small peak rises again, centered at 1 550 MeV and a peak value of roughly 4 nb/sr. Both the main peak and the smaller peak (should it indeed be one) appear very symmetrical. One point at the peak experiences a sharp drop but this could be due to statistical fluctuations.

The differential cross section has similar strengths to the ones measured for coherent $\pi^0\pi^0 d$ [7] and $\pi^0\eta d$ [8] production. Fig. 5.2 shows all three differential cross sections overlapped, depending on the center-of-mass energy. Coherent $\pi^0\pi^0 d$ production experiences its peak earlier than the other two

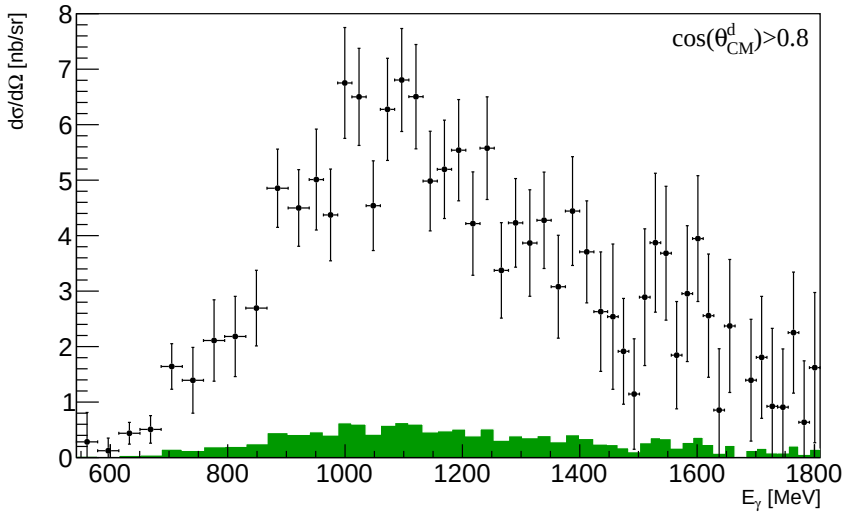

Figure 5.1: The measured differential cross section for coherent $\gamma d \rightarrow \pi^0\pi^0\pi^0 d$ in black data point. The green bars represent the systematical error.

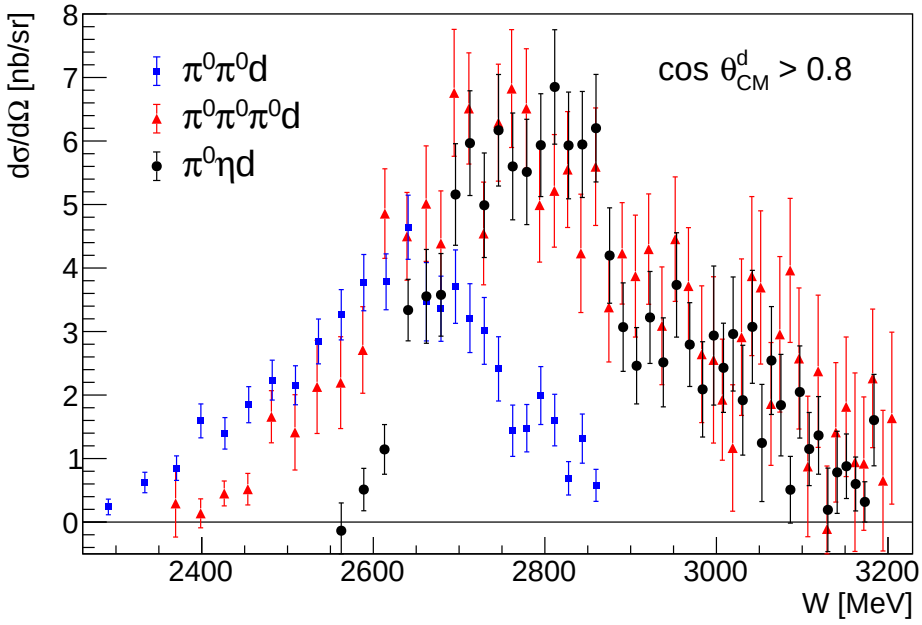

Figure 5.2: Comparison between the differential cross section for various coherent photoproduction reactions off the deuteron. Figure made by T. Jude (private communication).

around 2 650 MeV and also drops off when both $\pi^0\pi^0\pi^0 d$ and $\pi^0\eta$ production have their peak. Both reactions have a very strong similarity in peak position and following drop-off. All three reactions are notably different in the energy W where they begin to rise. This is a consequence of the different reaction thresholds which need to be met for photoproduction.

For coherent $\gamma d \rightarrow \pi^0\pi^0\pi^0 d$ production, relativistic kinematics can be used to calculate the threshold as

$$E_{\gamma,thr} = \frac{9m^2_{\pi^0}}{2m_d} + 3m_{\pi^0} \approx 449\,\text{MeV} \Rightarrow W_{thr} = \sqrt{2E_{\gamma,thr}m_d + m_d^2} \approx 2\,281\,\text{MeV} \tag{5.1}$$

As can be seen, the differential cross section rises about 100 MeV after the threshold has been met, but this could be simply due to the fact that for forward deuteron angles more energy must be transferred to the deuteron than what is available right at threshold.

One possible reason between the apparent similarities of $\pi^0\pi^0\pi^0 d$ and $\pi^0\eta d$ production could be the same kinematic model that was used to model the differential cross section in [8].

This model, seen in Fig. 5.3 consists of exciting one of the nucleons with the incident photon and by pion scattering the other one is also excited. The system consists then of a $N(1535)$ and a $\Delta(1232)$ resonance. While the $\Delta(1232)$ decays then into a neutron and a π^0 (branching ratio 99.4% [10]) the N(1535) can decay into a proton and a η and if both nucleons are similar enough in momentum, they can then coalesce into a deuteron again. The shape of such a model matches the measured cross section very well (see Fig. 2.12). There are two parts of this model, depending on whether the photon excites the proton or neutron first, but the main contribution comes from the proton excitation.

This model could similarly be used for the coherent $\pi^0\pi^0\pi^0 d$ production, since the $N(1535)$ decays with a branching ratio of 30 – 55% to the $N\eta$ state, but also with a branching ratio of 4 – 31 % to the

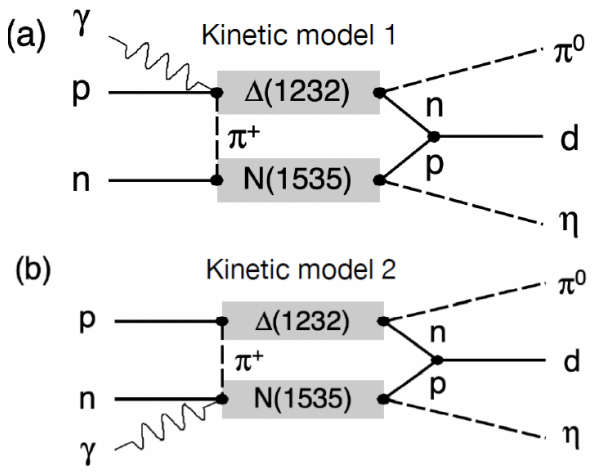

Figure 5.3: Model used to calculate the fits to the differential $\gamma d \rightarrow \pi^0 \eta d$ cross section. Figure taken from [8].

$N\pi\pi$ state [10]. Thus the same model could be used to explain both differential cross sections which would result in a similar shape very nicely. Of course this is no proof and a complete quantitative calculation of the model would need to be made in order to decide whether or not this model is actually viable.

5.2 Invariant mass dependent cross sections and phase space

π^0 π^0 invariant mass distribution Fig. 5.4 shows the invariant mass distributions for the 4 different W bins for the π^0 π^0 mass. Note that while the x-axis scaling is kept the same for all four diagrams, the y-axis scaling is adjusted for visibility, since the strength of the distributions varies greatly. Also the for the higher two W bins the invariant mass distributions, phase space simulations and systematic errors have been rebinned to half the number of bins than for the two lower energy bins. This is to reduce the statistical error of the data per bin.

The shape is similar among all energy bins, the only difference being that the width is greater for higher W. Otherwise all distributions experience a fast rise to a peak and then a slower fall which approaches zero. At their highest the distributions peak at about 80 pb/(sr*MeV) which is of course still small. The broadening of the shape with higher energy is expected since this allows for more momentum transferred to the pions resulting in higher angles between the different pions.

In general the distributions' shape matches the pure phase space simulations closely with nothing hinting at different processes.

π^0 π^0 π^0 invariant mass distribution The invariant mass distribution for the $3\pi^0$ invariant mass is shown in Fig. 5.5 together with systematical error and pure phase space. Again the x-axis is kept the same while y-axis was scaled with the distribution and two higher W bins have been rebinned.

The invariant mass distribution shows 2 peaks, their strength depending on center-of-mass energy. The first peak matches the nominal mass of the η meson while the second one moves with higher energy to higher invariant masses. The phase space matches the second peak in shape, becoming much broader with higher energy. The first peak is not be present in the third W bin (2 852–3 014MeV).

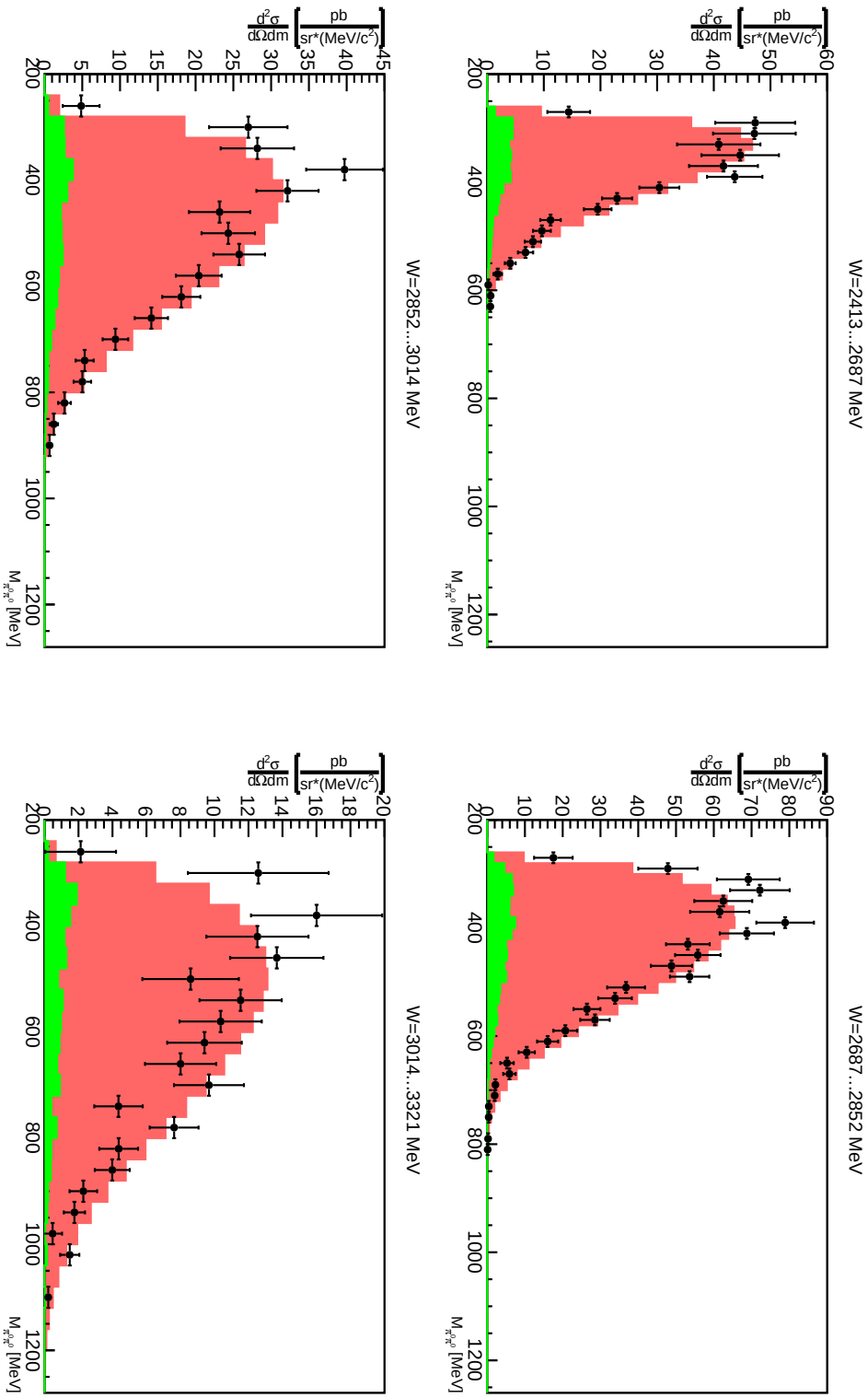

Figure 5.4: Distributions of the invariant mass of $\pi^0\,\pi^0$. Measured data in black, in shaded red bars a pure phase space simulations, in shaded green bars the systematic errors.

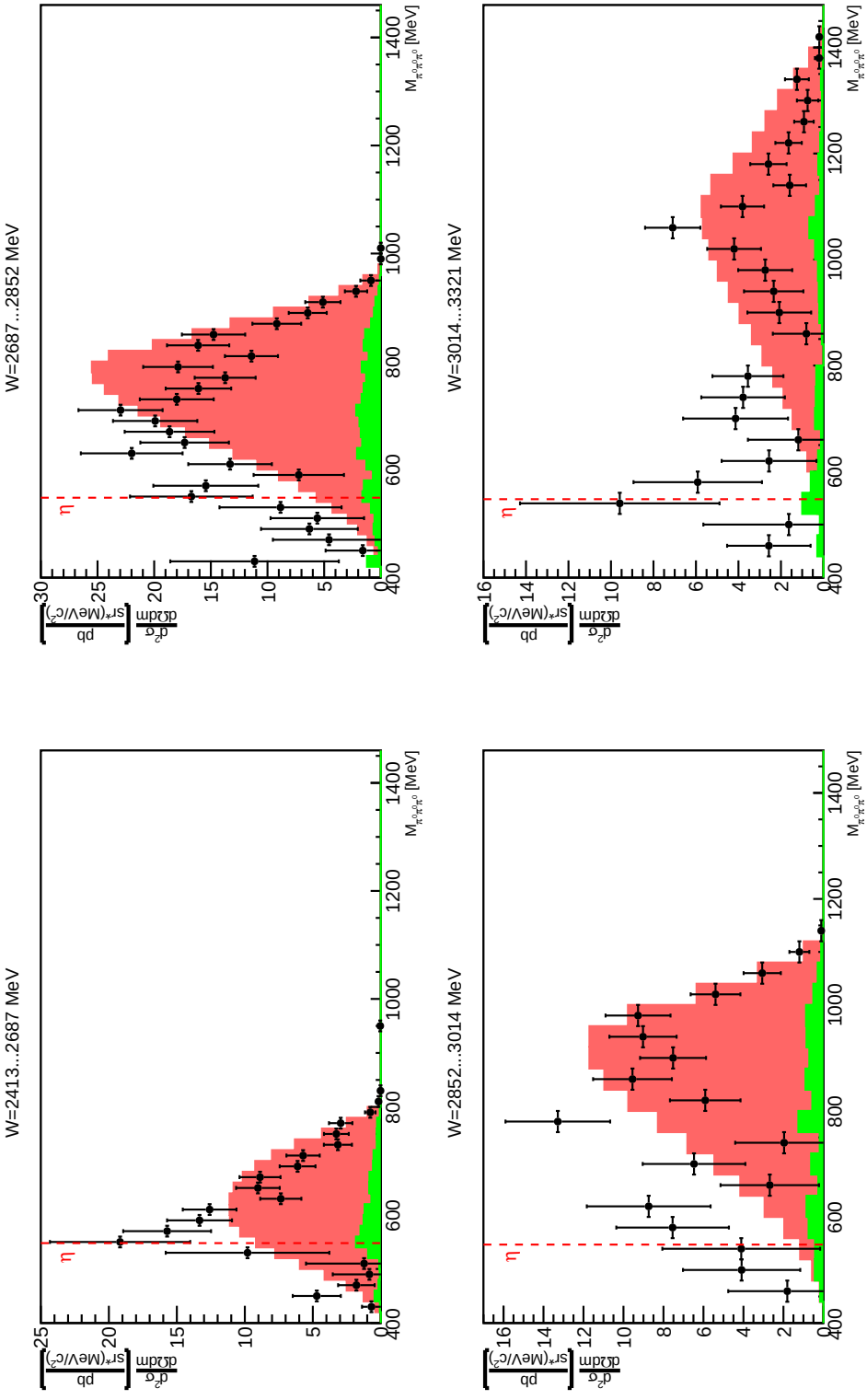

Figure 5.5: Distributions of the invariant mass of $\pi^0\,\pi^0\,\pi^0$. Measured data in black, in shaded red bars a pure phase space simulations, in shaded green bars the systematic errors. The red dotted line marks the nominal η mass.

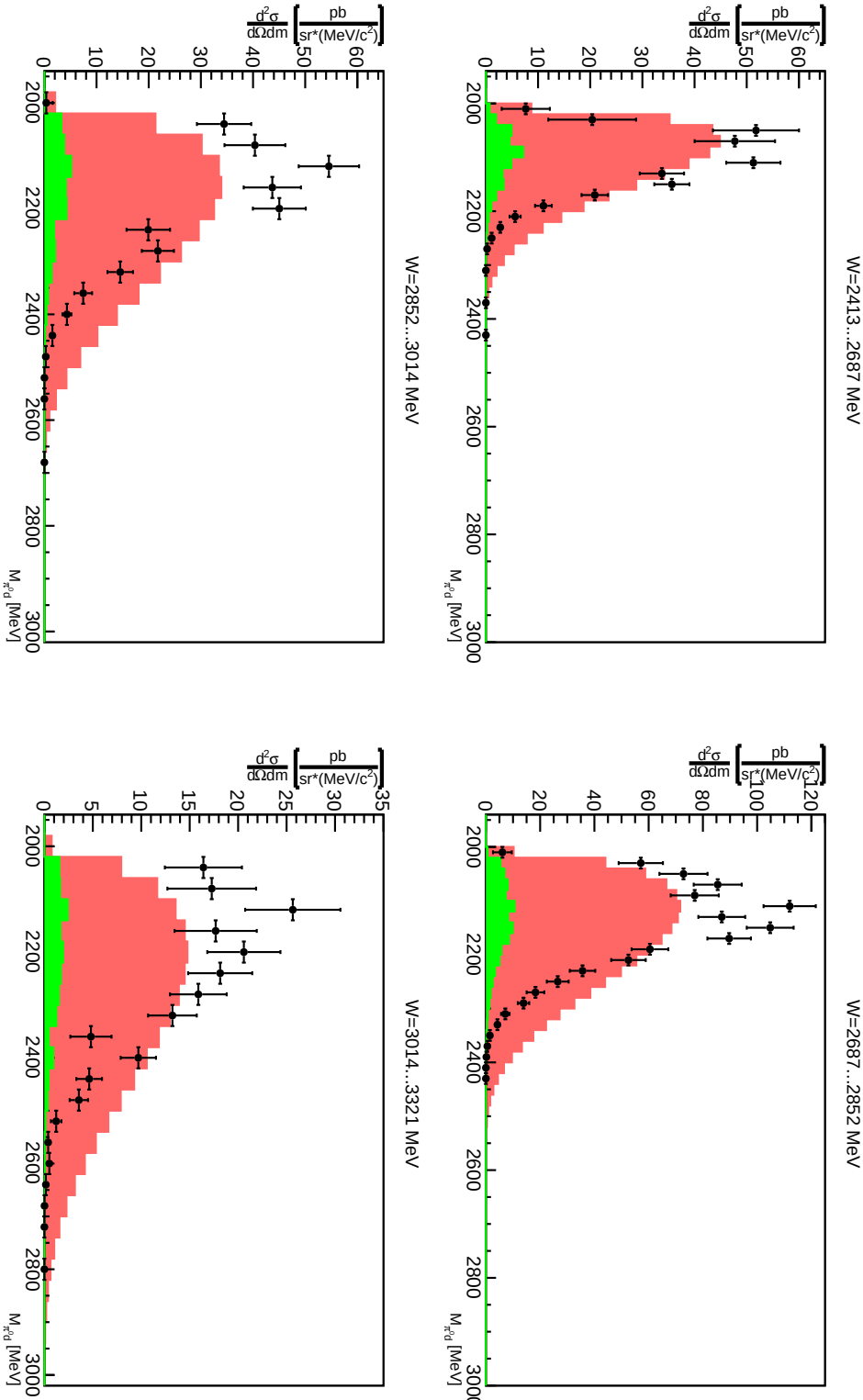

Figure 5.6: Distributions of the invariant mass of $\pi^0 d$. Measured data in black, in shaded red bars a pure phase space simulations, in shaded green bars the systematic errors.

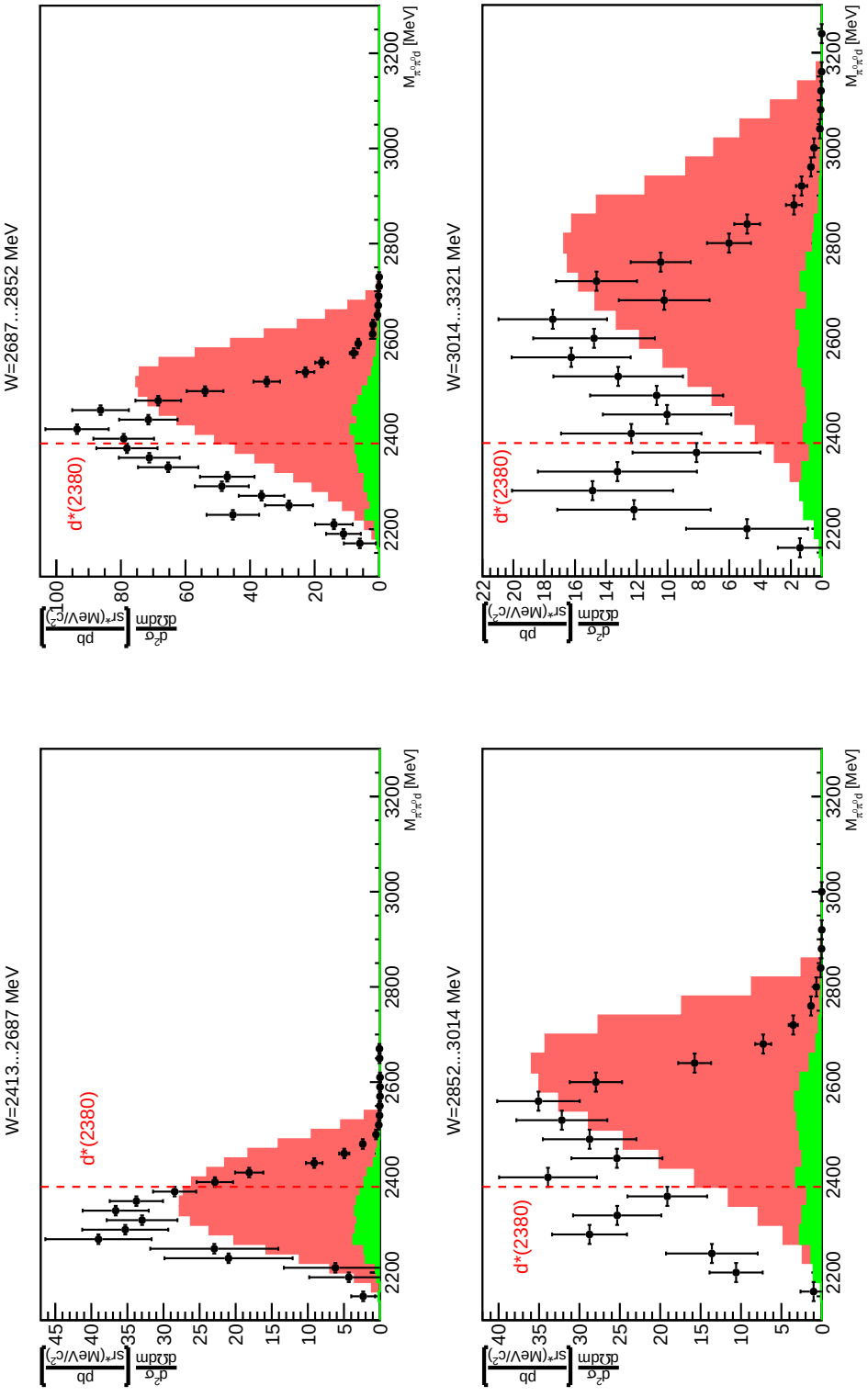

Figure 5.7: Distributions of the invariant mass of $\pi^0\pi^0 d$. Measured data in black, in shaded red bars a pure phase space simulations, in shaded green bars the systematic errors. The red dotted line marks the proposed $d^*(2380)$ dibaryon.

This could be a statistical effect or due to rebinning. Since the observed "peak" is very sharp and the statistical error is large enough, this could also originate from statistical fluctuations and not from an η decay. Nevertheless part of the spectrum can not be explained with pure phase space.

These invariant mass distributions may be a sum of phase space and the $\eta \rightarrow \pi^0\pi^0\pi^0$ decay. Coherent production of η could occur off the deuteron and subsequent decay into $3\pi^0$ which occurs with a branching ratio of $32.68 \pm 0.23\%$ [10]. This could be confirmed by measuring the coherent $\gamma d \rightarrow \eta d \rightarrow \gamma\gamma d$ reaction to confirm the strength of the coherent eta production from a different channel. However this reaction would also be severely suppressed due to the deuteron form factor [29].

$\pi^0 d$ invariant mass distribution Fig. 5.6 shows the invariant mass distributions, phase space simulations and systematic errors for the invariant $\pi^0 d$ mass. The distributions themselves have a similar shape to the π^0 π^0 distributions: A fast rise to a peak and a slower slope which approaches zero.

The shape is similar to the simulated phase space, although the phase space drops slightly slower with higher mass and does not reach the same peak height. However even though the simulation was scaled to match the data's integral, this choice is still somewhat arbitrary. Altogether no true hints for more complicated processes could be seen here. Noteworthy is that compared to the invariant mass distribution of coherent $\pi^0\pi^0 d$ production which shows a two peak structure [7], only one peak can be seen here. With this no further evidence for a sequential dibaryon decay can be obtained from these distributions.

$\pi^0\pi^0 d$ invariant mass distribution The last invariant mass distributions show the $\pi^0\pi^0 d$ invariant mass in Fig. 5.7. Lower energy bins show a relatively symmetrical peak in data which shifts to higher masses with higher energy. In the two W bins with the highest energy a secondary peak can be observed at around 2 300 MeV which does not seem to shift with energy.

The phase space simulation shows a different shape in all energy bins. It only has a single peak which becomes more asymmetrical with higher energy and the rising slope is longer than the falling slope, which is the opposite in data (for the second peak in data). The peak position is also notably higher in invariant mass for simulation compared to data. There also does not seem to be an enhancement at the proposed $d^*(2380)$ dibaryon.

The distribution seem to indicate at least two mechanisms needed: One which gives rise to the shape of the main peak and one which creates the stationary second peak after a certain energy threshold between 2 800 and 3 000 MeV has been met.

5.3 Summary

In this thesis the differential cross section $\mathrm{d}\sigma/\mathrm{d}\Omega_d$ and the invariant mass distributions for the $2\pi^0$, $3\pi^0$, $\pi^0 d$ and $2\pi^0 d$ masses have been successfully extracted for the coherent $\gamma d \rightarrow \pi^0\pi^0\pi^0 d$ reaction at forward deuteron angles $\cos\theta^d_{CM} > 0.8$.

With the help of mass cuts and a correction for quasi-free background, the differential cross section could be confirmed to be similar to previous results for coherent reactions measured at the BGOOD experiment. The strong similarity to the coherent $\gamma d \rightarrow \pi^0\eta d$ reaction hints at a similar production mechanism. It is possible that the same model that is used to explain the shape of the $\pi^0\eta d$ production could also give rise to the $\pi^0\pi^0\pi^0$ production but further confirmation is needed.

The invariant mass distributions can be divided into two groups: The first one consists of the $\pi^0\pi^0$ and $\pi^0 d$ invariant mass distributions. They both don't show any real discrepancies with pure phase space. The second one has such differences: In the $\pi^0\ \pi^0\ \pi^0$ distribution a η peak can be observed which hints at possible η production since a fitting decay channel would exist. In the $\pi^0\pi^0 d$ invriant mass distribution the main peak does not seem to fit to phase space and with higher center-of-mass energy a second peak is developed which hints at the presence of two different mechanisms different from pure phase space. The second peak at ca. 2 300 MeV does seem stationary in W but further confirmation would be needed since only 2 bins exist for it.

The sequential dibaryon decay model proposed in [7] could not be confirmed in the same invariant mass distributions and no hints for the presence of a $d^*(2380)$ resonance could be seen.

Going further, coherent ηd production could be explored at the same forward angles to investigate whether or not it truly causes the observed peak in $\pi^0\pi^0\pi^0$ invariant mass. This however would prove challenging, as the observed cross section is very small, in the order of 10 pb/(sr*MeV).

A further investigation is also needed to explain the appearance of two peaks in the $\pi^0\pi^0 d$ invariant mass distribution, one of which seems to move with W while the other seems stable.

It is altogether very curious that of four different invariant mass distributions two seem so close to an "easy" explanation and the other two further away but the coherent reaction channels seem to behave in a interesting manner, no matter which aspect is chosen to investigate.

APPENDIX **A**

Detection efficiencies depending on invariant masses

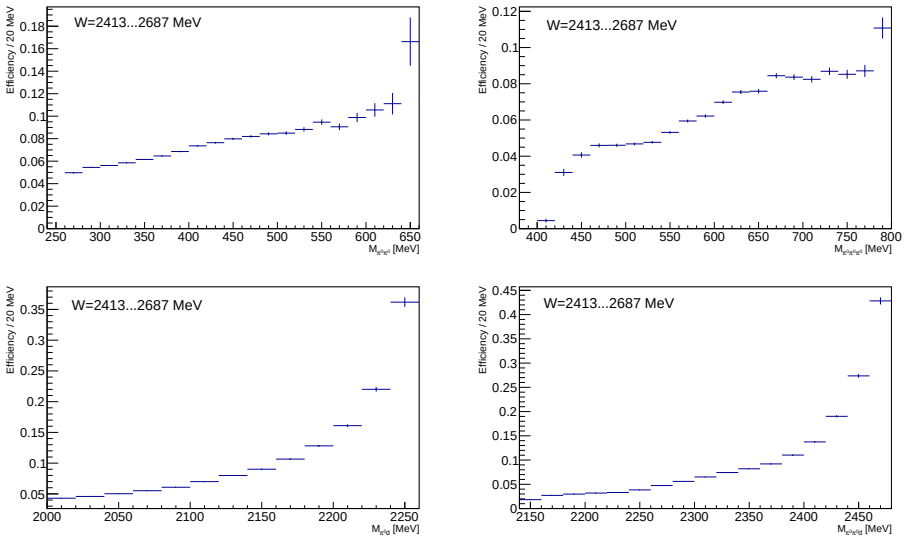

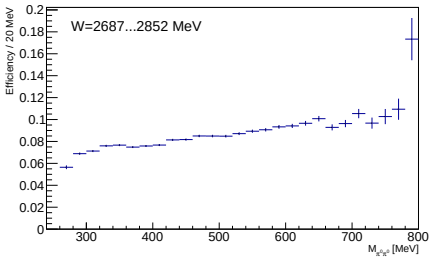
W=2687...2852 MeV
Efficiency / 20 MeV

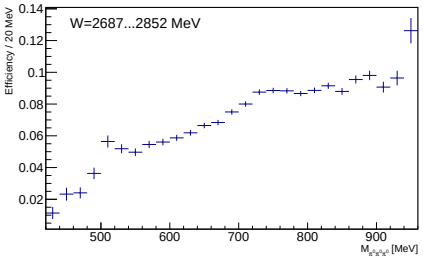
W=2687...2852 MeV
Efficiency / 20 MeV

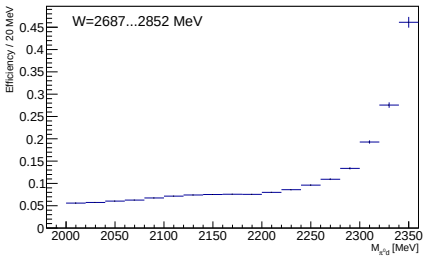
W=2687...2852 MeV
Efficiency / 20 MeV

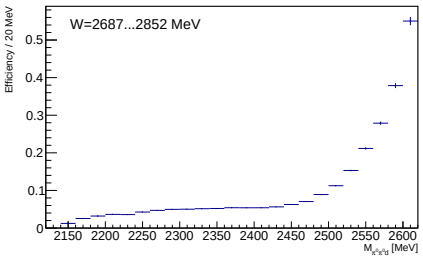
W=2687...2852 MeV
Efficiency / 20 MeV

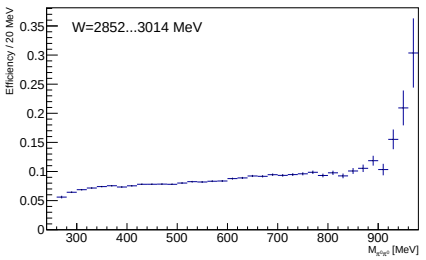
W=2852...3014 MeV
Efficiency / 20 MeV

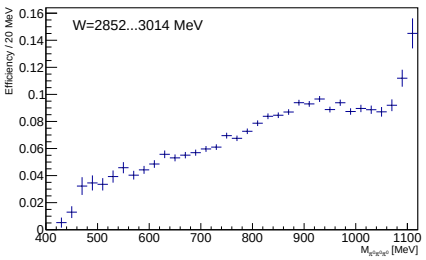
W=2852...3014 MeV
Efficiency / 20 MeV

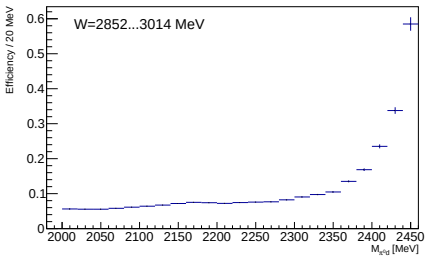
W=2852...3014 MeV
Efficiency / 20 MeV

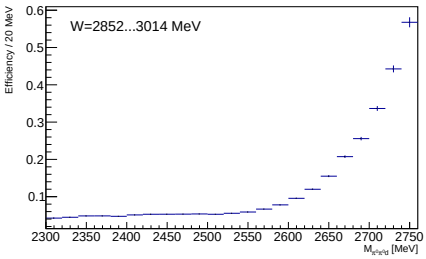
W=2852...3014 MeV
Efficiency / 20 MeV

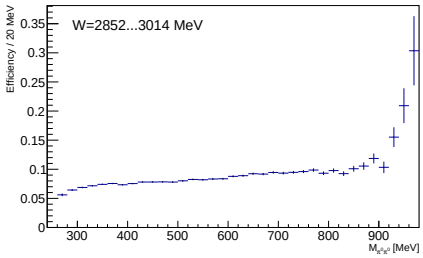
W=2852...3014 MeV
Efficiency / 20 MeV
0
0.05
0.1
0.15
0.2
0.25
0.3
0.35
300
400
500
600
700
800
900

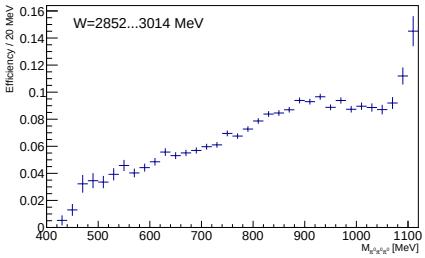
W=2852...3014 MeV
Efficiency / 20 MeV
0
0.02
0.04
0.06
0.08
0.1
0.12
0.14
0.16
400
500
600
700
800
900
1000
1100

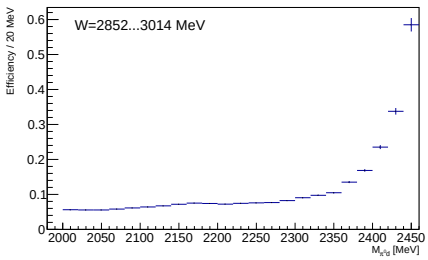
W=2852...3014 MeV
Efficiency / 20 MeV
0
0.1
0.2
0.3
0.4
0.5
0.6
2000
2050
2100
2150
2200
2250
2300
2350
2400
2450

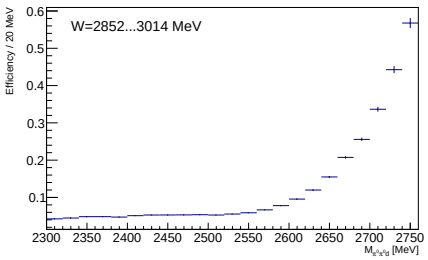
W=2852...3014 MeV
Efficiency / 20 MeV
0.1
0.2
0.3
0.4
0.5
0.6
2300
2350
2400
2450
2500
2550
2600
2650
2700
2750

Bibliography

[1] D. Griffiths, *Introduction to Elementary Particles*, Second, Revised Edition, Weinheim: Wiley-VCH, 2008, ISBN: 978-3-527-40601-2.

[2] M. Lubej, *Study of $B \to KK\ell\nu_\ell$ decays at Belle*, PhD thesis: University of Ljubljana, 2018, URL: https://repozitorij.uni-lj.si/IzpisGradiva.php?lang=eng&id=105432.

[3] H. Clement, *On the history of dibaryons and their final observation*, Progress in Particle and Nuclear Physics **93** (2017) 195, ISSN: 0146-6410, URL: https://www.sciencedirect.com/science/article/pii/S0146641016300771.

[4] P. Adlarson et al., *Evidence for a New Resonance from Polarized Neutron-Proton Scattering*, Phys. Rev. Lett. **112** (20 2014) 202301, URL: https://link.aps.org/doi/10.1103/PhysRevLett.112.202301.

[5] T. Ishikawa et al., *First measurement of coherent double neutral-pion photoproduction on the deuteron at incident energies below 0.9 GeV*, Physics Letters B **772** (2017) 398, ISSN: 0370-2693, URL: https://www.sciencedirect.com/science/article/pii/S0370269317302848.

[6] T. Ishikawa et al., *Non-strange dibaryons studied in the $\gamma d \to \pi^0\pi^0 d$ reaction*, Physics Letters B **789** (2019) 413, ISSN: 0370-2693, URL: https://www.sciencedirect.com/science/article/pii/S0370269318309857.

[7] T. Jude et al., *Evidence of a dibaryon spectrum in coherent $\pi^0\pi^0 d$ photoproduction at forward deuteron angles*, Physics Letters B **832** (2022) 137277, ISSN: 0370-2693, URL: https://www.sciencedirect.com/science/article/pii/S0370269322004117.

[8] A. C. Figueiredo et al., "Coherent $\pi^0\eta d$ photoproduction at forward deuteron angles measured at BGOOD", 2024, URL: https://arxiv.org/abs/2405.09392.

[9] M. Gell-Mann, *THE EIGHTFOLD WAY: A THEORY OF STRONG INTERACTION SYMMETRY*, (1961), URL: https://www.osti.gov/biblio/4008239.

[10] S. Navas et al., *Review of particle physics*, Phys. Rev. D **110** (2024) 030001.

[11] M. Gell-Mann, *A schematic model of baryons and mesons*, Physics Letters **8** (1964) 214, ISSN: 0031-9163, URL: https://www.sciencedirect.com/science/article/pii/S0031916364920013.

[12] G. Zweig, *An SU_3 model for strong interaction symmetry and its breaking; Version 2*, (1964), URL: https://cds.cern.ch/record/570209.

[13] F. J. Dyson and N.-H. Xuong, *$Y = 2$ States in Su(6) Theory*, Phys. Rev. Lett. **13** (26 1964) 815, URL: https://link.aps.org/doi/10.1103/PhysRevLett.13.815.

[14] P. Adlarson et al., *Abashian-Booth-Crowe Effect in Basic Double-Pionic Fusion: A New Resonance?*, Phys. Rev. Lett. **106** (24 2011) 242302, URL: https://link.aps.org/doi/10.1103/PhysRevLett.106.242302.

[15] M. Bashkanov, H. Clement and T. Skorodko, *Examination of the nature of the ABC effect*, Nuclear Physics A **958** (2017) 129, ISSN: 0375-9474, URL: https://www.sciencedirect.com/science/article/pii/S0375947416302962.

[16] A. Abashian, N. E. Booth and K. M. Crowe, *Possible Anomaly in Meson Production in $p + d$ Collisions*, Phys. Rev. Lett. **5** (6 1960) 258, URL: https://link.aps.org/doi/10.1103/PhysRevLett.5.258.

[17] A. Fix and H. Ahrenhövel, *Double-pion photoproduction on nucleon and deuteron*, Eur. Phys. J. A **25** (2005) 115.

[18] M. Egorov and A. Fix, *Coherent $\pi 0 \pi 0$ photoproduction on lightest nuclei*, Nuclear Physics A **933** (2015) 104, ISSN: 0375-9474, URL: https://www.sciencedirect.com/science/article/pii/S0375947414004965.

[19] T. Ishikawa et al., *Coherent photoproduction of the neutral-pion and η-meson on the deuteron at incident energies below 1.15 GeV*, Phys. Rev. C **105** (4 2022) 045201, URL: https://link.aps.org/doi/10.1103/PhysRevC.105.045201.

[20] M. Egorov and A. Fix, *Coherent $\pi^0\eta$ photoproduction on s-shell nuclei*, Phys. Rev. C **88** (5 2013) 054611, URL: https://link.aps.org/doi/10.1103/PhysRevC.88.054611.

[21] M. Egorov, *Coherent photoproduction of two neutral pseudoscalar mesons on light nuclei*, Phys. Rev. C **101** (6 2020) 065205, URL: https://link.aps.org/doi/10.1103/PhysRevC.101.065205.

[22] T. Yao, *Model for the Interaction $p + p \rightarrow d + \pi^+$ in the BeV Region*, Phys. Rev. **134** (2B 1964) B454, URL: https://link.aps.org/doi/10.1103/PhysRev.134.B454.

[23] I. Bar-Nir et al., *Analysis of the reaction $np \rightarrow d\pi+\pi-$ below 3.5 GeV/c*, Nuclear Physics B **54** (1973) 17, ISSN: 0550-3213, URL: https://www.sciencedirect.com/science/article/pii/055032137390062X.

[24] S. Alef et al., *The BGOOD experimental setup at ELSA*, Eur. Phys. J. A **56** (2020) 104.

[25] G. Scheluchin, *$\Lambda(1405)$ photoproduction with the BGO-OD Experiment*, PhD thesis: Rheinische Friedrich-Wilhelms-Universität Bonn, 2017, URL: https://hdl.handle.net/20.500.11811/8373.

[26] O. Freyermuth, *Studies of ω Photoproduction off Proton at the BGO-OD Experiment*, PhD thesis: Rheinische Friedrich-Wilhelms-Universität Bonn, 2017, URL: https://hdl.handle.net/20.500.11811/7263.

[27] J. Allison et al., *Recent developments in Geant4*,
Nuclear Instruments and Methods in Physics Research Section A: Accelerators, Spectrometers, Detectors and Associated Equipment **835** (2016) 186, ISSN: 0168-9002, URL:
https://www.sciencedirect.com/science/article/pii/S0168900216306957.

[28] S. Alef et al., $K^+\Lambda$ *photoproduction at forward angles and low momentum transfer*,
Eur. Phys. J. A **57** (2021).

[29] J. Weiß et al., *Exclusive measurement of coherent η-photoproduction from the deuteron*,
Eur. Phys. J. A **11** (2001) 371.

List of Figures

List of Tables